Global and Planetary Change 256 (2026) 105170

Contents lists available at ScienceDirect

Global and Planetary Change

journal homepage: www.elsevier.com/locate/gloplacha

Research Article

Immediate and delayed biotic and environmental responses to the carbon cycle perturbation at the onset of OAE 1a – Insights from a new high-resolution record from the Western Tethys☆

Cristina Sequero[a,*], Sandro Froehner[b], José Manuel Castro[c], Ginés A. De Gea[c],
María Luisa Quijano[d], B. David A. Naafs[e], Richard D. Pancost[e]

[a] *Departamento de Geodinámica, Estratigrafía y Paleontología, Universidad Complutense de Madrid, 28040 Madrid, Spain*
[b] *Department of Environmental Engineering, University of Parana, 81531-980 Curitiba, Brazil*
[c] *Departamento de Geología, Universidad de Jaén and CEACTEMA, 23071 Jaén, Spain*
[d] *Departamento de Química Inorgánica y Orgánica and CEACTEMA, Universidad de Jaén, 23071 Jaén, Spain*
[e] *Organic Geochemistry Unit, School of Chemistry, University of Bristol, BS8 1TS Bristol, UK*

ARTICLE INFO

Editor: Dr. Maoyan Zhu

Keywords:
OAE 1a onset
Carbon cycle perturbation
High-resolution study
Biotic response
Environmental changes
OJP-volcanism

ABSTRACT

The onset of the early Aptian Oceanic Anoxic Event (OAE 1a) was an interval of rapid global environmental change, linked to a major perturbation of the carbon cycle. A complex response of the biotic and environmental system occurred, ultimately triggered by volcanism of the Ontong-Java Plateau. Here we present a new high-resolution study of the very onset of OAE 1a (ca. 80 kyr), obtained through integration of C-isotope stratigraphy, total organic carbon (TOC) contents, elemental geochemistry and biomarkers, in order to examine the nature and timing of changes in the carbon cycle, biota and the environmental system. This work provides new evidence for an early response of the biotic and environmental system, which predates the more generalized development of oceanic anoxia and widespread increase in primary productivity. The early response took place as soon as few kyrs after the initiation of the carbon cycle perturbation, whereas the major change occurred some 29 kyr later. A probable injection of methane postdates the onset of OAE 1a by 6 kyr, likely triggered by early stages of volcanism and/or sill intrusions into organic-rich sediments. These results provide new insights into the analysis of the onset of OAE 1a, and indicates that future research at higher resolution is required in order to better understand the complex interplay of Earth system processes in response to increases in pCO_2.

1. Introduction

Oceanic anoxic events (OAEs) represent major perturbations in global environmental and biotic systems, typically associated with increased atmospheric CO_2 concentrations and hyperthermal conditions, ultimately derived from perturbations in the global carbon cycle (Jenkyns, 2010). OAE 1a, which occurred at ca. 120 Ma (early Aptian; Gradstein et al., 2020), is one of the most prominent OAEs and has been studied over the last several decades (e.g., Menegatti et al., 1998; Erba, 2004; Immenhauser et al., 2005; Huck et al., 2010, 2011; Jenkyns, 2010, 2018; Lorenzen et al., 2013; Bottini et al., 2015; Naafs and Pancost, 2016; Castro et al., 2021, 2025; Bauer et al., 2021, 2024; Percival et al., 2021, 2025; Sun et al., 2025). This event has a global character, with sedimentary, biotic and environmental impacts on land and oceans (e.g., Skelton, 2003; Hay, 2017). Its main signature is the C-isotope record (Menegatti et al., 1998), with a negative excursion (CIE) at its base followed by a longer positive phase, with a total duration of the entire anoxic event of ca. 1.4 Myr (e.g., Erba et al., 2015; Martínez-Rodríguez et al., 2024). These major C-isotope shifts have allowed the subdivision of the event into segments (Menegatti et al., 1998), which are the robust basis for global correlation of OAE 1a.

A complex pattern of biogeochemical and climatic feedback mechanisms has been associated with OAE 1a through the study of different geochemical, biotic and sedimentary proxies, along with climate

---

☆ This article is part of a Special issue entitled: 'Oceanic Anoxic Event' published in Global and Planetary Change.

* Corresponding author.

E-mail addresses: cristinasq92@gmail.com (C. Sequero), froehner@ufpr.br (S. Froehner), jmcastro@ujaen.es (J.M. Castro), gadegea@ujaen.es (G.A. De Gea), lquijano@ujaen.es (M.L. Quijano), David.Naafs@bristol.ac.uk (B.D.A. Naafs), R.D.Pancost@bristol.ac.uk (R.D. Pancost).

https://doi.org/10.1016/j.gloplacha.2025.105170
Received 13 February 2025; Received in revised form 14 October 2025; Accepted 5 November 2025

models, all of them paired with different age models (e.g., Erba et al., 2015; Adloff et al., 2020; Percival et al., 2025). The most widely accepted interpretations invoke the emplacement of Ontong-Java Plateau (OJP) volcanism in the central Pacific Ocean as the main driver for the palaeoenvironmental and biotic perturbations of OAE 1a (e.g., Erba, 1994; Jones and Jenkyns, 2001; Jenkyns, 2010; Matsumoto et al., 2024). This large volcanic activity is consistent with perturbations documented in the osmium isotope record, $p\mathrm{CO}_2$ reconstructions (Tejada et al., 2009; Méhay et al., 2009; Bottini et al., 2012; Naafs et al., 2016; Martínez-Rodríguez et al., 2021), and other proxies worldwide (e.g., Erba et al., 2015; Percival et al., 2021, 2025). The associated injection of massive amounts of CO_2 into the atmosphere-ocean system linked to this volcanic activity caused global warming and intensification of the hydrological cycle (e.g., Beerling and Royer, 2002; Tejada et al., 2009; Méhay et al., 2009; Jenkyns, 2010; Mutterlose et al., 2014; Bottini et al., 2015; Erba et al., 2015; Naafs and Pancost, 2016; Naafs et al., 2016). This led to a eutrophication of the oceans, enhancement of primary productivity, widespread elevated burial rates of organic matter, and development of generalized anoxia in oceanic bottom waters (e.g., Kump et al., 2000; Jenkyns, 2010; Aguado et al., 2014; Bottini et al., 2015; Bauer et al., 2021, 2024). Methane release has also been invoked as an additional light carbon source triggering or amplifying climate warming during OAE 1a, with corresponding environmental impacts (e.g., Weissert and Erba, 2004; Méhay et al., 2009; Erba et al., 2010, 2015; Bottini et al., 2012; Naafs et al., 2016; Adloff et al., 2020; Percival et al., 2025).

The OAE 1a as a whole, with a duration of ca. 1.4 Myr (e.g., Erba et al., 2015; Martínez-Rodríguez et al., 2024), has been the focus of a large number of studies during the last several decades (e.g., Erba, 1994, 2004; Menegatti et al., 1998; Méhay et al., 2009; Erba et al., 2010, 2015; Lorenzen et al., 2013; Erba et al., 2015; Castro et al., 2019, 2021; Bauer et al., 2021, 2024; Percival et al., 2021, 2025; Sun et al., 2025). However, only few studies focus on the onset of OAE 1a are carried out (Méhay et al., 2009; Bauer et al., 2022), which is globally associated with a significant negative shift in the C-isotope record (both $\delta^{13}C_{org}$ and $\delta^{13}C_{carb}$) (e.g., Menegatti et al., 1998; Jenkyns, 2010; Erba et al., 2010), that defines the base of the C3 isotope segment of Menegatti et al. (1998). The investigation of this initial phase of the OAE 1a is crucial for understanding the complex feedback mechanisms controlling this event, in which both long- and short-term environmental changes took place (e.g., Kuhnt et al., 2011; Aguado et al., 2014; Castro et al., 2019). In this regard, although previous studies have focused on the mechanisms acting during the onset of OAE 1a (e.g., Méhay et al., 2009; Erba et al., 2015; Bauer et al., 2021), higher-resolution studies are needed to test the different hypotheses proposed for the triggering of OAE 1a, and refine the timescale and causal relationships of the immediate environmental perturbations (e.g., Hay, 2017; Bauer et al., 2024).

The Carbonero section represents an excellent opportunity to obtain new, detailed insights into the onset of OAE 1a, since it provides a complete and expanded record of the early Aptian, arising from high sedimentation rates in a pelagic trough with high subsidence (e.g., Martín-Chivelet et al., 2002; de Gea et al., 2008a; see next section). The identification of the OAE 1a in the Carbonero section is well constrained by the combined C-isotope stratigraphy and biostratigraphy (nannofossils, foraminifera, radiolarian) (e.g., Aguado et al., 1993; de Gea et al., 2008b; Castro et al., 2019), and the age model is based on C-isotope correlation with the nearby Cau section with robust cyclostratigraphy (e.g., Martínez-Rodríguez et al., 2024). In particular, the C3 isotope segment here is represented by a thick (19 m) interval that represents a time span of 230 kyr (Martínez-Rodríguez et al., 2024), and mainly consists of black shales, dark marls and radiolarites. In this work, we present a new high-resolution study focused on the very onset of OAE 1a (lowest part of the C3 segment, ca. 7 m-thick interval), spanning ca. 80 kyr (Martínez-Rodríguez et al., 2024). This study integrates C-isotope stratigraphy, TOC, biomarkers and elemental proxies (major and trace elements) at an unprecedented high resolution, in order to gain additional insights into the biotic and environmental changes that occurred during the initiation of OAE 1a in a pelagic basin from the Western Tethys.

2. Geological setting

The Carbonero section is situated in the Jaén province, southeastern Spain (geographic coordinates: base, 37° 33′ 39.40“N, 3° 48’ 2.27”W; top, 37° 33′ 41.85“N, 3° 48’ 4.08”W) (Fig. 1A, B). These deposits belong to the External Zones of the Betic Cordillera (Fig. 1B), which include thick successions (> 3000 m thick) of carbonates and siliciclastics that were deposited in shallow-marine (Prebetic Platform) to hemipelagic/pelagic domains (Subbetic Basin) that represent sedimentation in the Southern Iberian Palaeomargin (SIP) (Fig. 1B, C) (e.g., Martín-Chivelet et al., 2002; Vera, 2004). During Aptian times, pulses in extensional tectonics triggered by the initiation of the seafloor spreading in the North Atlantic led to the configuration of the SIP into separate subsiding pelagic sub-basins controlled by listric faults, surrounded by uplifted sectors where shallow-marine sedimentation took place (Fig. 1D) (Martín-Chivelet et al., 2002; de Gea et al., 2008a). The Carbonero section represents deposition in a pelagic trough of the Subbetic Basin, in a highly subsident sector that led to an expanded and complete record of the early Aptian sedimentation, considerably thicker than in other sections worldwide (see Fig. 6 in Castro et al., 2019). Palaeogeographic reconstructions situate the Carbonero sector at a palaeolatitude of 20–25°N (Masse et al., 1993), within the northern part of the equatorial arid belt (Chumakov et al., 1995) (Fig. 1C).

The Carbonero section contains a thick succession of intercalated marls, marly limestones, black shales and radiolarites (Fig. 2A) (e.g., Aguado et al., 1993; de Gea et al., 2008a, 2008b; Castro et al., 2019). These deposits correspond to the Carbonero Formation (Molina, 1987), which lies on the Berriasian-Barremian marly limestones of the Carretero Formation (de Gea et al., 2008a; Fig. 2A). Originally proposed as stratotype of the Carbonero Formation, Molina (1987) identified three members for this unit at Carbonero site, named the lower, middle and upper member, with different lithological characteristics (details on the lithostratigraphy are contained in de Gea et al., 2008a). The interval analysed in this work is situated in the lower part of the middle member, which comprises deposition of black shales with local intercalation of mudstones at the base and the top of the interval, and punctual cinerite levels (Fig. 2A). The initiation of the negative C- isotope excursion that globally defines the onset of the OAE 1a (onset CIE) coincides here with deposition of the black shales (at ca. 28 m in Fig. 2A).

The expression of the OAE 1a in the middle member of the Carbonero Formation is identified by combined information mainly from C-isotope stratigraphy (identification of the Menegatti et al. (1998) isotope segments C3 to C6) (Castro et al., 2019) and calcareous nannofossils (Aguado et al., 1993; de Gea, 2004; de Gea et al., 2008b). The calcareous nannofossil record is mostly restricted to the lower and uppermost parts of the Carbonero section, and allowed the identification of the NC5, NC6A, NC6B and NC7A zones of Bralower et al. (1995), based on the first record of the specimens *Hayesites irregularis* and *Eprolithus floralis*, and the last record of *Conusphaera rothii* (Fig. 2A). The complete stratigraphic distribution of *C. rothii* and *E. floralis* is partially limited due to the lack of carbonates in some parts of the section. The nannoconid crisis event is also recognized (Fig. 2A).

3. Materials and methods

3.1. *Fieldwork description and sampling*

The Carbonero section reported by Castro et al. (2019) was re-sampled between 27.15 and 34.33 m (7.18 m-thick interval), starting one metre below the very onset of the negative C-isotope excursion (uppermost C2 segment) for $\delta^{13}C_{org}$, in order to clearly characterize the C-isotope shift, and following through the lower 6.38 m of the C3

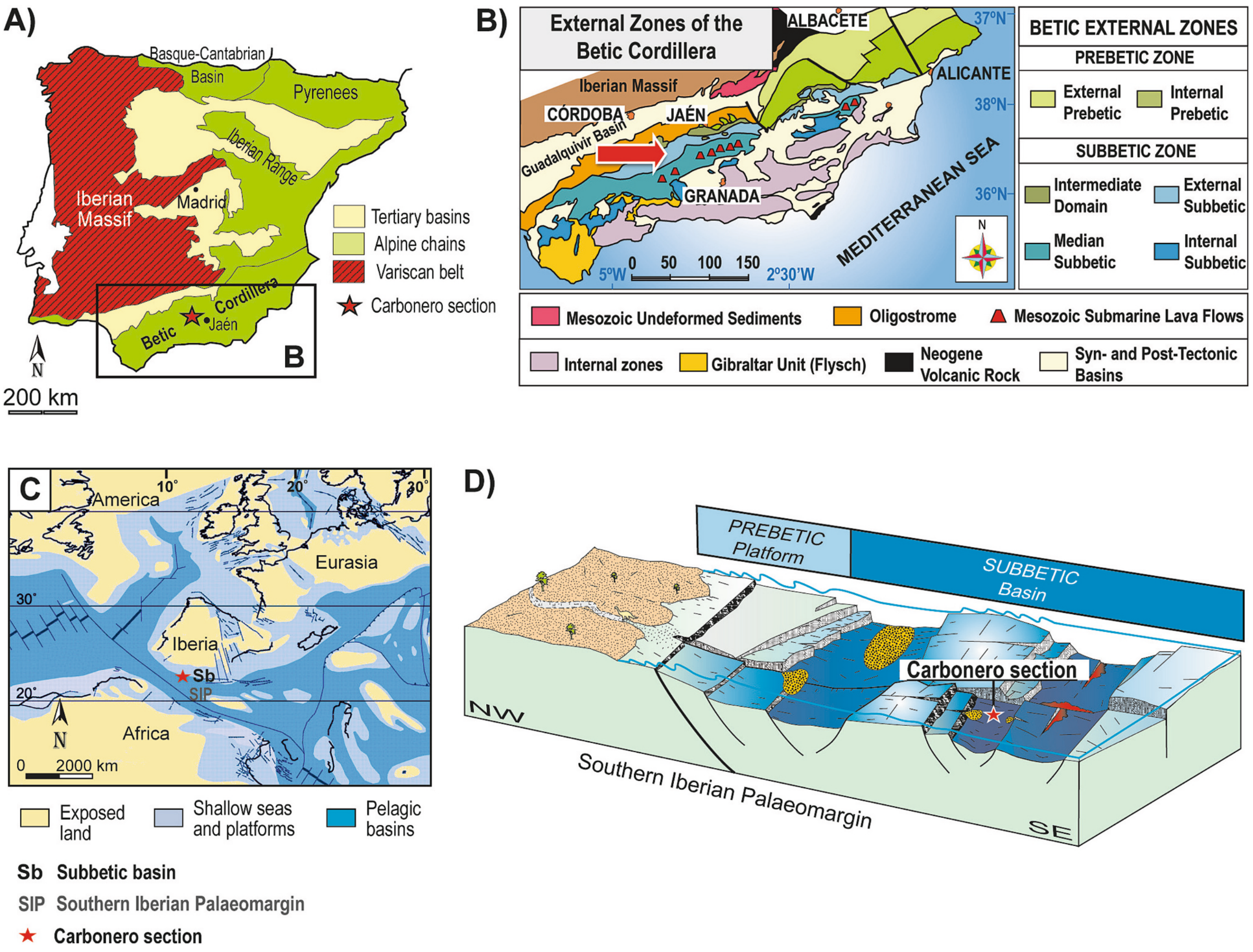

Fig. 1. A-B) Geographic location of the Carbonero section (red star) in southern Spain (A), and geological map of these southern areas of the Iberian Peninsula (Betic External Zones) (B) (adapted from Castro et al., 2019, 2021). The deposits of the Carbonero section (red arrow in B) correspond to the External Subbetic Zone. C) Palaeogeographic reconstruction of the Western Tethys during the early Aptian (~120 Ma; modified from Masse et al., 2000), with the location of the Carbonero section. D) Depositional model of the Southern Iberian Palaeomargin during the early Aptian. The Carbonero section (red star) represents deposition in a pelagic trough surrounded by listric faults (modified from de Gea et al., 2008a). (For interpretation of the references to colour in this figure legend, the reader is referred to the web version of this article.)

segment (Fig. 2). A total of 85 samples were taken for bulk geochemical analyses (see Tables S1 to S3 in the Supplementary Material, SM). Of these, 68 samples were taken for $\delta^{13}C_{org}$ (Table S1 in SM). The average space of sampling is 2 cm at the very onset of the negative CIE (between 28 and 28.8 m), and 25 cm for the rest of the interval. In order to characterize the environmental and biotic perturbations starting from the onset of the CIE through the lower 6.38 m-thick interval of the C3 segment, a number of samples were selected for TOC content, elemental geochemistry (major and trace elements) and biomarker analyses. A total of 39 samples were selected for elemental geochemistry and TOC content (Table S2 in SM), at an average sampling resolution of 5 cm between 28 and 28.8 m, and of 25 cm for the rest of the interval. Finally, a total of 25 samples, at a resolution of 25 cm at the very onset of the CIE and 50 cm for the rest of the interval, were selected for biomarker analyses (Table S3 in SM).

3.2. Bulk geochemistry

3.2.1. Carbon isotope stratigraphy

The C-isotope analyses of the total organic fraction ($\delta^{13}C_{org}$) were conducted at the Stable Isotope Laboratory (SIDI) of the University Autónoma of Madrid (Spain). Removal of carbonate from the samples was previously done by applying 3 % HCl during 24 h. The samples were analysed using a Carlo Erba 1108 elemental analyser coupled to an IRMS VG Isochrom in continuous flow mode. The $\delta^{13}C_{org}$ data obtained here refine previously published carbon isotope stratigraphy in Castro et al. (2019), by obtaining a C-isotope curve at a much higher resolution (18 samples in Castro et al. (2019) vs. 68 samples taken for this study; Fig. 2). These data were obtained in three rounds between 2021 and 2022, two of them encompassing from the uppermost C2 to the very onset of the negative CIE (i.e., from 27.15 to 29 m; triangle and circle symbols in Fig. 2B), and the other one for the rest of the interval (diamond symbols in Fig. 2B) (Table S1 in SM). Cinerite levels have been avoided during sampling. For the interval corresponding to the uppermost C2 to the very onset of the negative CIE, the $\delta^{13}C_{org}$ data trend is represented as a regression line of the data obtained by the LOESS method (Cleveland and Devlin, 1988; Jacoby, 2000), using PAST software, in order to avoid artificial data fluctuations originated by instrumental deviation, instantaneous depositional perturbations and/or C-isotope fractionation at decarbonation during sample preparation (see SM for further details of the method used). The Vienna PeeDee Belemnite (VPDB) international standard was used to calibrate the results, with a precision better than 0.1 ‰.

3.2.2. Major and trace elements

Analyses for major and trace element concentrations were performed

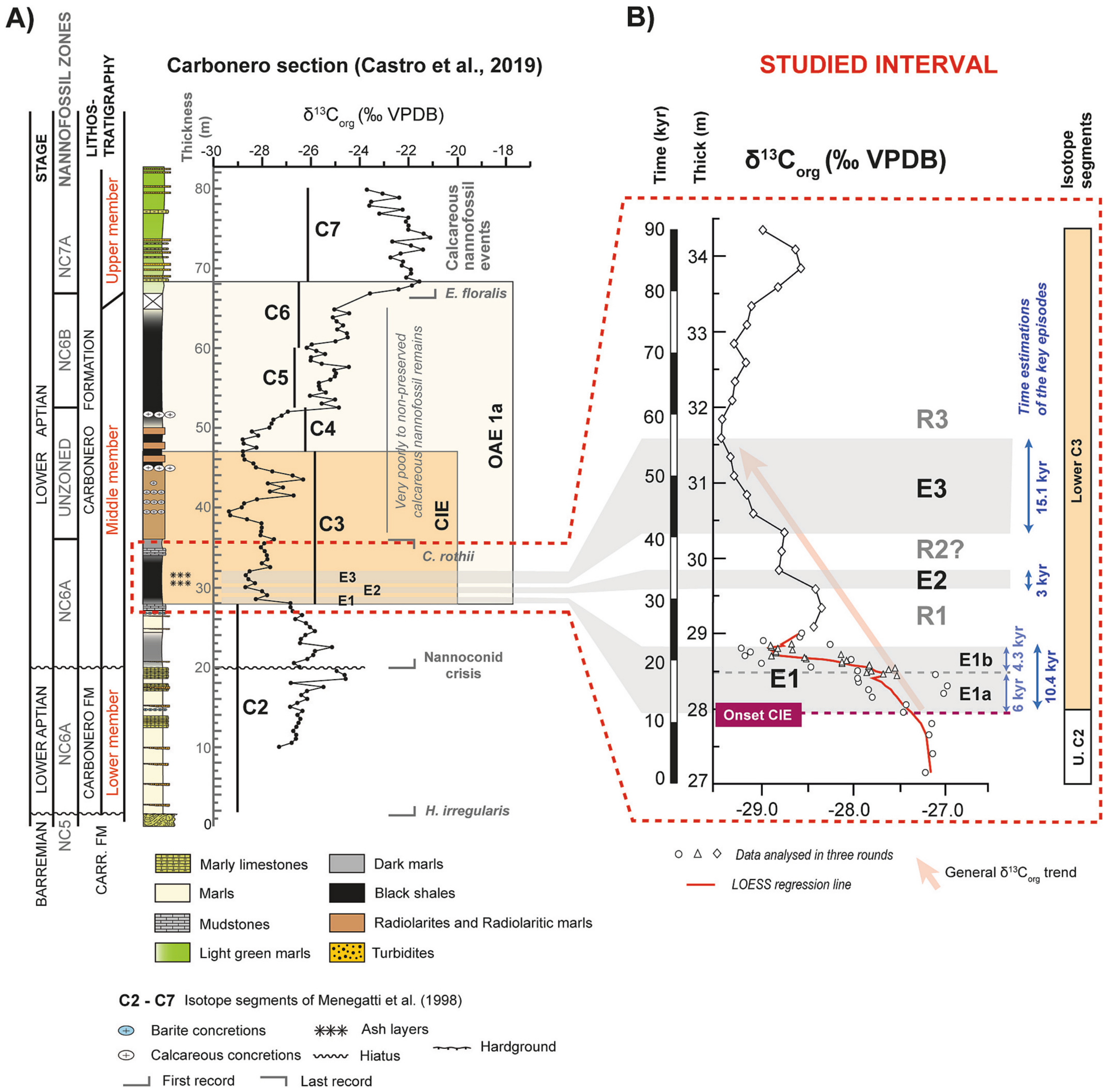

Fig. 2. A) Stratigraphy, biostratigraphy and C-isotope stratigraphy of Carbonero section from Castro et al. (2019). B) High-resolution $\delta^{13}C_{org}$ profile and time estimations (kyr) for the key episodes at the studied interval.

at the Centro de Instrumentación Científica (CIC) of the University of Granada (Spain). Powdered samples (0.1 g per sample) were acid-clean digested in a combination of HNO^{3+} and HF^{+} (ratio 2:3) at high temperature (180 °C) and pressure (200 psi) in a Teflon-lined vessel for 30 min. The samples were then evaporated to dryness, and subsequently re-dissolved in 100 ml of 4 vol. HNO_3. Element concentrations were determined by inductively coupled plasma-mass (ICP-MS; model Perkin Elmer NEXION 300D) and optical emission spectrometry (ICP-OES; model Perkin-Elmer Optima 8300) for trace and major element concentrations, respectively. For ICP-MS, the spectrometer was equipped with quartz torch, nickel sampler and skimmer cones, a peristaltic pump (maintaining 1 ml min^{-1} sample uptake rate), a cross-flow type pneumatic nebulizer, and a double pass Scott-type spray chamber. All the ICP-MS standards were prepared from ICP single element standard solutions (Merck quality) after appropriate dilution with 10 % HNO_3. For calibration, two sets of multielement standards containing all the ICP-MS analyses of interest at five levels concentrations were prepared using Rhodium as internal standard. For estimating the detection limits, procedural blanks ($3 * \sigma$; $n = 6$) were < 0.03 ppb for Ir, < 0.01 ppb for Cu, < 2.68 ppb for Zn, < 0.75 ppb for As, and < 0.72 ppb for Pb. The analytical precision was better than ±5 % in all cases. In case of ICP-OES analyses, a set of monoelement standards specific of the Perkin Elemer model were used for calibration.

Elemental concentrations are normalized to Al (Element/Al), in order to compensate for the dilution effect (e.g., Calvert and Pedersen, 2007). Elemental concentrations and ratios (major and minor) are shown in Table S2. The Al-normalized concentrations are also compared to the average crustal rock element abundance or Average Shale Value (ASV) (Wedepohl, 1991; Brumsack, 2006), to evaluate increased or depleted concentrations.

3.2.3. Total organic carbon (TOC)

TOC analyses were carried out at the Centro de Asistencia a la Investigación (CAI) of the University Complutense of Madrid (Spain). TOC content was determined using a Total Organic Carbon Shimadzu TOC-VCSH Analyser coupled with a Shimadzu SSM-5000 A solids module, by Combustion and Infrared (IR) Detection. The TOC concentration was determined by subtracting the inorganic carbon (IC) concentration from the total carbon (TC) in each sample. Firstly, the sample is combusted at high temperature to form CO_2. After that, the carbon dioxide, along with other combustion products, are entrained in the carrier gas and then cooled and dehydrated before reaching the NDIR (non-dispersive infrared) detector cell. The peak area is proportional to the concentration of TC from IC. TOC concentration is expressed as a weight percent (wt%) (Table S2), and with a precision better than 0.1 %.

3.3. Biomarkers

Biomarker analyses were conducted at the University of Jaén (Spain). Bulk rock samples (selected from those for TOC analyses) were collected in the field following several steps: first, the sampling locations were cleaned by removing superficial altered sediments (most probably affected by the weathering); secondly, the samples were collected with tweezers and wrapped in aluminium foil to avoid any contamination during handling and transportation. Once in the laboratory, in order to remove any contamination during handling, the samples surfaces were cleaned with dichloromethane (DCM). The samples were then crushed into small pieces of approximately 1 cm with an agate mortar, and afterwards milled into powder using a Pulverisette 5 agate mill operating under 400 rpm for 5 min (previously cleaned with acetone and DCM). After that, the organic components within rock powders were extracted using a Pressurised Liquid Extraction System model ASE350, previously cleaned using methanol (MeOH) and DCM for 4 cycles with an extraction volume of 40 ml/cycle and a total duration of 2 h. The pulverised samples (13 g) were extracted within 24 h, by adding approximately 1 g of diatomea earth in each sample to provide porosity to the sample for a better extraction of the liquids. The extraction was carried out in a mix of DCM and methanol (DCM/MeOH 4:1, *v*/v). After extraction, copper turnings were added to the total lipid extracts (TLEs) for 24 h to remove elemental sulphur, and then evaporated using nitrogen. TLE separation was performed by flash column chromatography using silica gel and a sequential elution with hexane, dichloromethane:hexane (1:3, v/v) and methanol, obtaining three fractions that contain saturated hydrocarbons, aromatic hydrocarbons and polar compounds, respectively.

The saturated hydrocarbon fractions (containing *n*-alkanes, steranes and hopanes) were analysed with a gas chromatography–mass spectrometry (GC–MS) at the Centro de Instrumentación Científica y Técnica of the University of Jaén (CICT-UJA, Spain), using a Thermo DSQ II gas chromatograph connected to a Thermo Trace Ultra mass spectrometer. The GC was fitted with an on-column injector and a fused (Sigma Aldrich) silica capillary column, with the 5-MS reference phase (30 m × 0.25 mm × 0.25 μm film thickness), using helium as the carrier gas. Once the samples (in hexane) were injected at 70 °C, the oven was subsequently programmed to 130 °C at 20 °C/min and then to 300 °C at 4 °C/min, where the temperature was held for 20 min. Biomarkers were identified using *Xcalibur* software, by comparing the mass spectra and retention times with those reported in the literature (e.g., Peters et al., 2005). Biomarker ratios were calculated by peak integration of the identified biomarkers associations, and are shown in Table S3.

4. Results

4.1. Age model and C-isotope stratigraphy

The high-resolution $\delta^{13}C_{org}$ profile provided here for the uppermost C2 to the lower part of C3 segments, which encompasses the very onset of the OAE 1a, refines the previously published C-isotope curve in Castro et al. (2019) (Fig. 2A), which permits a new, more nuanced, subdivision of the C-isotope record into three negative excursions (E1 to E3), each followed by a recovery interval (R1 to R3) (Fig. 2B). Moreover, the E1 excursion has been divided into a C-isotope negative excursion (E1a) and a C-isotope negative spike (E1b). This subdivision is based on a change in the slope (Fig. 3), which evolves from −1.2685 in E1a, to −0.2244 in E1b.

Based on the average sedimentation rate calculated for the Carbonero section by Castro et al. (2019) (i.e. 6.3 cm/kyr, derived from the estimated 300 kyr duration of the C3 interval), the analysed interval (from 27.15 to 34.33 m) in the Carbonero section corresponds to ca. 114 kyr. More recent estimates for the duration of the C3 segment are either longer (434 kyr, Beil et al., 2020; 485 kyr, Charbonnier et al., 2023), or shorter (104 kyr, Steuber et al., 2022). Cyclostratigraphy from an hemipelagic succession from the Western Tethys, the Cau core (Martínez-Rodríguez et al., 2024), indicates an intermediate duration for the C3 segment of 230 kyr, with an average sedimentation rate of 8.26 cm/kyr. We use this age estimation, which implies that the 7.18 m study interval for $\delta^{13}C_{org}$ (i.e. from the uppermost C2 to the lower C3 segment) has a duration of ca. 87 kyr. Accordingly, the 6.38 m-thick interval analysed for TOC content, elemental geochemistry and biomarkers (i.e., the lower C3 segment, which represents the very onset of OAE 1a), yields a duration of 77 kyr. Thus, assuming a constant sedimentation rate for the Carbonero section in the analysed interval (mainly represented by black shales, with no evidence of condensed sedimentation, turbidites and/or hiatus), we can infer the timing of the newly recognized C-isotope excursions and their recovery intervals (Fig. 3 and Table 1).

The C-isotope excursion E1 at the very onset of the C3 segment is the most abrupt, with an amplitude of 2 ‰ over 0.86 m, which is estimated to be ca. 10.4 kyr (Fig. 3 and Table 1). E1 has been in turn divided into a first C-isotope negative excursion (E1a) over 0.5 m (6 kyr), and a following C-isotope negative spike (E1b) over 0.36 m (4.3 kyr), based on a change in the slope mentioned above (Fig. 3). After a recovery interval (R1) of the C-isotope excursion E1, a second and less pronounced C-isotope excursion, E2, has also been considered (with a less well-defined recovery interval R2), showing an amplitude of 0.34 ‰ over 0.25 m, and a temporal estimation of 3 kyr. Finally, the C-isotope excursion E3 has an amplitude of 0.69 ‰ over a thickness of 1.25 m (15.1 kyr), reaching the most negative C-isotope signal. These values, assuming constant sedimentation rates as previously explained, indicate that the negative excursions are successively less abrupt.

4.2. Elemental geochemistry and TOC content

Total organic carbon (TOC) contents and major and trace element concentrations provide useful information about the depositional environment, such as changes in productivity, redox conditions, or variations in continental input and/or nutrient supply. In this work, we use several proxies to infer changes in productivity (TOC, P/Al), terrestrial input (Rb/Al, K/Al, Zr/Al) and redox conditions (U/Th, Ni/Co, V/Cr, V/Al, U/Al, Cr/Al, and V/Sc) (e.g., Jones and Manning, 1994; Bodin et al., 2007; Calvert and Pedersen, 2007; Martínez-Ruiz et al., 2015) (Fig. 4).

Redox sensitive trace elements (RSTE) (U/Th, Ni/Co, V/Cr, V/Al, U/Al, Cr/Al, and V/Sc) (Calvert and Pedersen, 2007) show generally parallel trends through the section (Fig. 4B). The RSTEs record rather stable values close to the Average Shale Value (ASV) (Brumsack, 2006) within the oxic field during E1 and E2, followed by a gradual enrichment during E3, with maxima around the minimum $\delta^{13}C_{org}$ values, being diagnostic

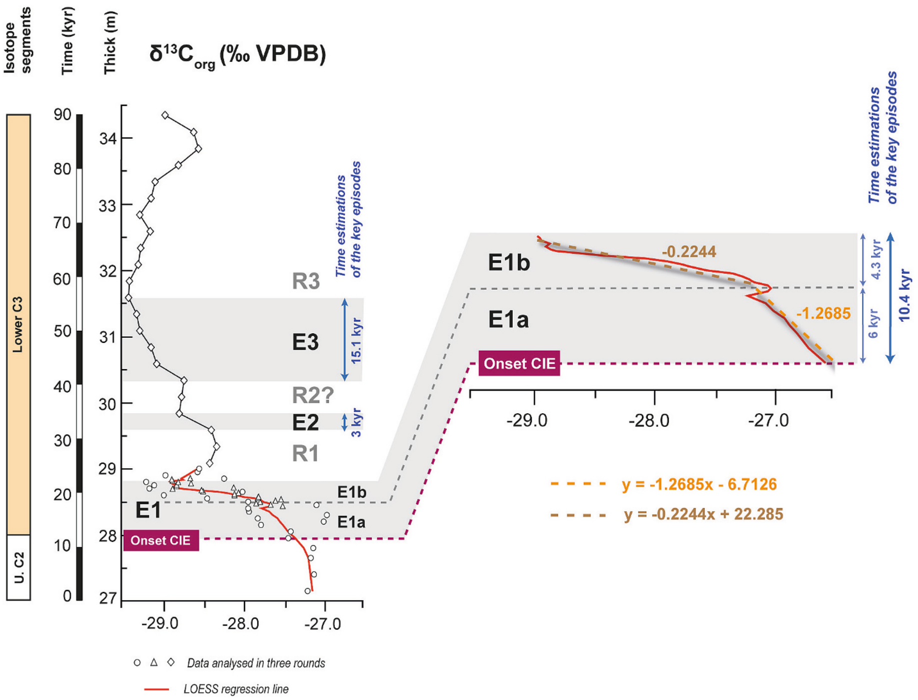

Fig. 3. Subdivision of the E1 interval in E1a and E1b excursions based on a calculated change in the slope. Time estimations (kyr) for the key C-isotope excursions identified are indicated.

Table 1
Thickness (m) and timespan (kyr) of the C-isotope excursions (E1, E2 and E3) and the recovery intervals (R1 to R3) within the analysed lower part of the C3 isotope segment (Menegatti et al., 1998) in the Carbonero section. [1]The thickness for the C3 isotope segment is based on Castro et al. (2019), and the timespan is based on Martínez-Rodríguez et al. (2024).

	C3 isotope segment[1]	Analysed interval (lower part of C3)						
		E1		R1	E2	R2?	E3	R3
		E1a	E1b					
Thickness (m)	19	0.5	0.36	0.77	0.25	0.5	1.25	2.5
Timespan (kyr)	230	6.05	4.35	9.31	3.02	6.05	15.12	30.24

of sediment deposition under oxygen depleted (e.g., V/Cr) or anoxic (e.g., Ni/Co) conditions (indicated in Fig. 4B as “oxic/dysoxic” and “sub-oxic/anoxic”, respectively). After E3, concentrations decrease gradually to values typical of sediment deposition under well oxygenated conditions.

P/Al ratios and TOC contents are used here as indicators of productivity (Fig. 4A). P/Al ratios generally have values below ASV (mean 0.006) throughout the interval, but with a significant enrichment during E3 up to the ASV concentration (ca. 0.09). They parallel TOC contents, which range from 0.5 to 2 wt% during E1-E2, abruptly increase to 3.8 wt % at the onset of E3, and then decrease gradually up-section. Variations in continental inputs have been quantified by Rb/Al and K/Al ratios for fluvial sources, and Zr/Al for aeolian (Martínez-Ruiz et al., 2015) (Fig. 4A). These record generally parallel trends, with low and unstable values during E1. During R1 and E3, they record two slight increases in two steps, with values near (K/Al) or above (Rb/Al) the ASV, followed by a decrease in the upper part of the section.

4.3. *Biomarker distributions*

The groups of biomarkers that dominate in the extracted saturated hydrocarbon fraction are hopanes, steranes and *n*-alkanes. Here, selected biomarker ratios (Fig. 5) have been calculated to complement information regarding productivity, the source of the organic matter (continental vs marine) and environmental (redox) conditions; as well as estimating thermal maturity.

4.3.1. *n-alkanes*

n-alkanes are the most abundant saturated hydrocarbons in these samples, and in our analytical window, they range from n-C_{13} to n-C_{37}. Short-chain (low molecular weight) *n*-alkanes are typically associated with marine organic matter sources, whereas long-chain (high molecular weight) *n*-alkanes reflect terrigenous input (Eglinton and Hamilton, 1967), although those attributions are less robust at high thermal maturity (see Section 4.3.2). The relative abundances of the low-molecular-weight (LMW; $< C_{22}$) and the high-molecular-weight (HMW; $> C_{24}$) components are quantified here in the HMW/(HMW + LMW) ratio ($[n\text{-}C_{25} + n\text{-}C_{26} + n\text{-}C_{27} + n\text{-}C_{28} + n\text{-}C_{29}] / [(n\text{-}C_{25} + n\text{-}C_{26} + n\text{-}C_{27} + n\text{-}C_{28} + n\text{-}C_{29}) + (n\text{-}C_{17} + n\text{-}C_{18} + n\text{-}C_{19} + n\text{-}C_{20} + n\text{-}C_{21})]$) (Peters et al., 2005), with peak areas determined from m/z 57 (see Fig. S1 in SM). This ratio exhibits very little variability in this section, decreasing slightly from E1 up to the middle part of E3, and then increasing upwards (Fig. 5).

4.3.2. *Hopanes*

Hopanes are pentacyclic triterpenoids derived from a wide range of bacteria (e.g., Rohmer et al., 1984; Belin et al., 2018). They are present in all of the samples, ranging in carbon number from C_{27} to C_{35} (Table S3 and Fig. S1 in SM). Hopanes in the Carbonero section reveal a relatively high mature distribution, with 17α,21β(H) isomer dominating over the

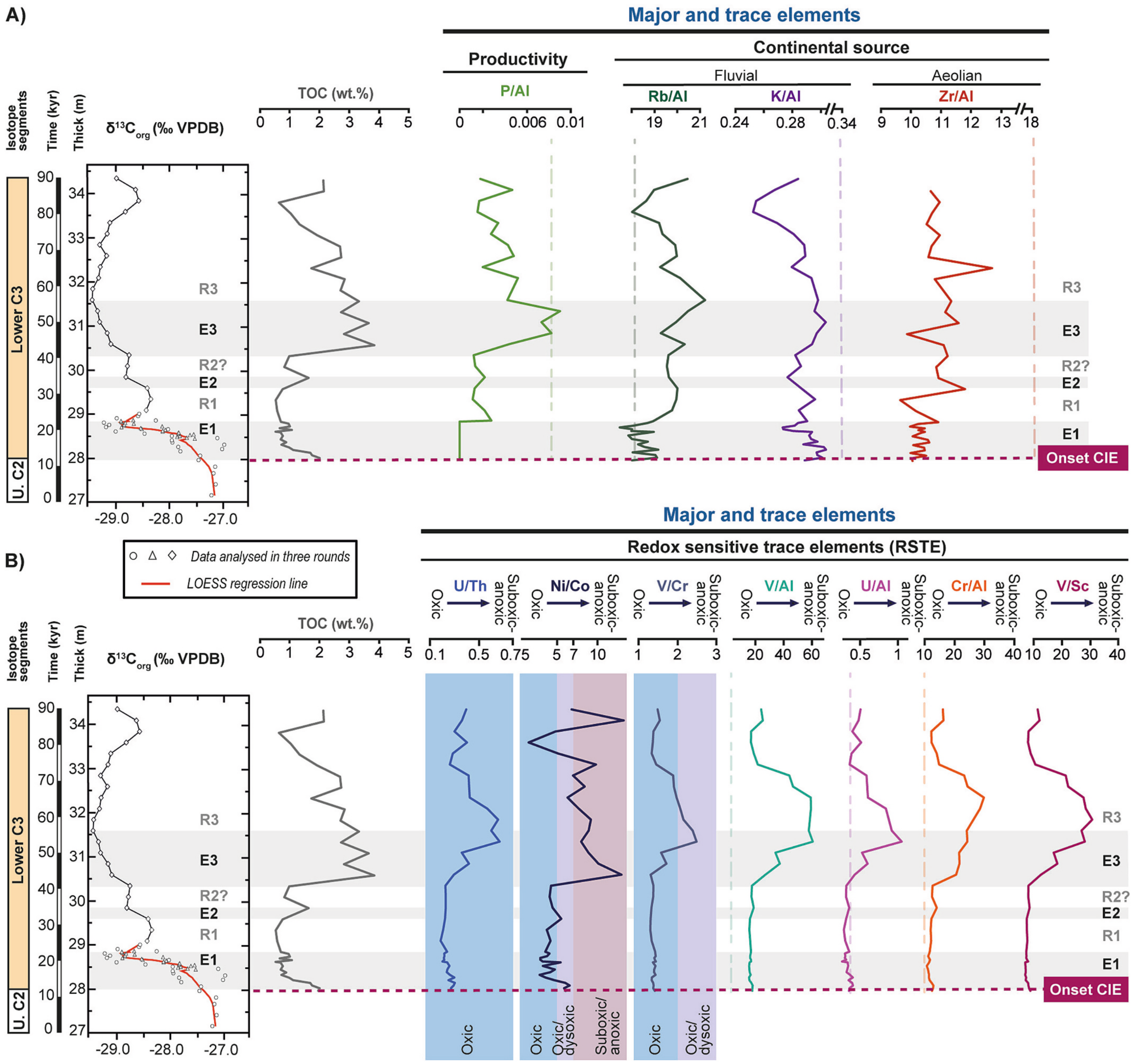

Fig. 4. (A) (B) $\delta^{13}C_{org}$, TOC and selected major and trace element ratios for the studied interval. Al-normalized elements in major elemental concentrations (P, Rb, K, Zr) are presented as Element/Al ratios, and in trace elements (U, V, Cr,) as Element/Al x 10^{-4} ppm. Dashed vertical lines represent the average shale value (ASV; Brumsack, 2006). U/Th, Ni/Co and V/Cr ratios are plotted according to the different oxygen-content bands sensu Jones and Manning (1994).

17β,21α(H) isomer and the 17β,21β(H) isomer being absent (Peters et al., 2005). Below, we explain the three selected ratios that have been calculated to examine the distribution of hopanes through the study interval, shown in Fig. 5.

We use the C_{30} βα/(βα + αβ) hopane ratio, which quantifies the relative abundance of the C_{30}-hopane 17β,21α(H) and 17α,21β(H) isomers, to assess thermal maturity. This ratio has an average value of 0.2, characteristic of high thermal maturity but in a pre-oil generation window of maturity (vitrinite reflectance shows values at or near 0.6; Peters et al., 2005).

The C_{31} 2-Me-hopane index (2-MHI) reflects changes in the bacterial community, and is defined by the abundance of C_{31} 2-methylhopanes relative to total C_{31} hopanes: 100 x C_{31} 2-Me-hopane/(C_{31} 2-Me-hopane + C_{31} hopane) (Summons et al., 1999). The areas are calculated from the *m/z* 191 and 205 mass chromatograms for αβ-hopanes and 2α-methylhopanes, respectively (Summons et al., 1999). This ratio, interpreted to reflect an ecological response to low oxygen or changes in the nitrogen cycle (Ricci et al., 2017; Naafs et al., 2022), is low but gradually increases during E1-R1, sharply rises to ca. 30 % at the base of E3, and then decreases through E3 before increasing to a second peak during R3.

Finally, the hopane-based homohopane index (HHI), which reflects changes in redox conditions at the sediment-water interface, is defined as 100 x C_{35} hopane/(C_{31} hopane - C_{35} hopane), with all areas calculated from the *m/z* 191 mass chromatogram (Bishop and Farrimond, 1995; Peters et al., 2005). This ratio is rather variable in the section with three maxima – at the end of E1, at the mid part of E3, and mid part of R3 – although all values are relatively low.

4.3.3. Steranes

A group of C_{27} to C_{29} steranes occur in all the samples. The three

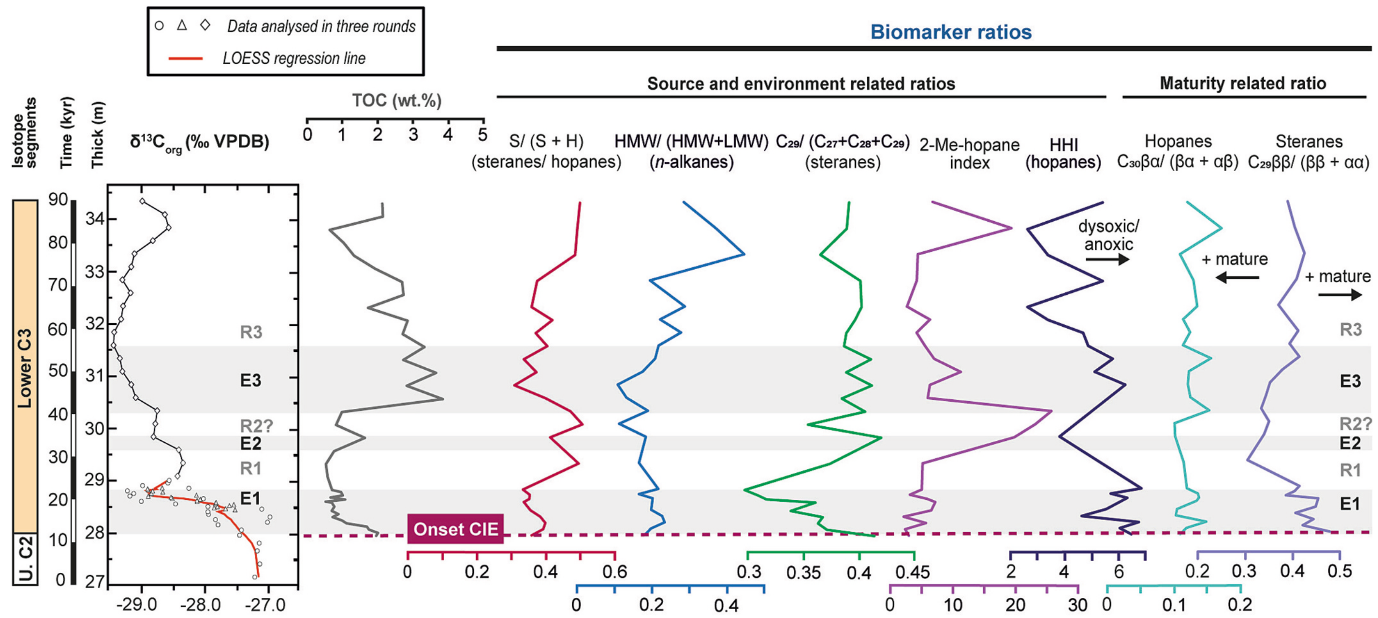

Fig. 5. Selected biomarker ratios as proxies for reconstructing sources of organic matter, environmental conditions and thermal maturity.

common “regular steranes” are all present: C_{27}-cholestane, C_{28}-ergostane and C_{29}-stigmastane (Table S3 and Fig. S1 in SM). The C_{29}-sterane $\beta\beta/(\beta\beta + \alpha\alpha)$ ratio, which quantifies the relative abundance of the four epimers $5\alpha(H),14\alpha(H),17\alpha(H),20R$; $5\alpha(H),14\alpha(H),17\alpha(H),20S$; $5\alpha(H),14\beta(H),17\beta(H),20S$ and $5\alpha(H),14\beta(H),17\beta(H),20R$, is a widely used indicator of thermal maturity. In the Carbonero section, it has an average value of 0.4, characteristic of high thermal maturity (values near to oil generation between 0.4 and 0.6; Peters et al., 2005), similar to that inferred from hopane distributions.

Sterane distributions can reflect either the relative abundance of aquatic vs terrestrial inputs and/or changes in algal distributions. In settings receiving significant terrestrial input, the C_{29}-steranes are normally attributed to terrestrial higher plants (Huang and Meinschein, 1979), whereas in settings without substantial terrestrial influence, the C_{27}-steranes have been suggested to represent contribution of red algae while the C_{28}- and C_{29}-steranes preferentially reflect green algae (Schwark and Empt, 2006). The relative distribution of these three steranes across the interval has been quantified through the $C_{29}/(C_{27} + C_{28} + C_{29})$ ratio (Huang and Meinschein, 1979). This ratio shows a sharp decrease during E1, followed by an increase during R1-E2, and then high, variable values up-section (Fig. 5).

Finally, we use the sterane/hopane (S/(S + H)) ratio [C_{27-29} steranes/(C_{27-29} steranes + C_{27-35} hopanes)] (calculated here using integrations from the m/z 217 and 191 mass chromatograms, respectively) to further examine changes in OM source. It reflects the relative contribution of eukaryotic (algal) to bacterial sources (e.g., Peters et al., 2005; Belin et al., 2018), and thus can be indicative of changing algal productivity. It shows steady values during E1, highest values during R1-R2, followed by a decrease at the base of E3 and a gradual increase up-section.

5. Discussion

5.1. The onset of the OAE 1a in previous studies and the significance of this new high-resolution record

Constraining the timing and triggering mechanisms for Phanerozoic OAEs is crucial for understanding the response of the Earth system to global carbon cycle perturbations, which requires more detailed high-resolution records (e.g., Jiang et al. (2025) for the PETM). For the OAE 1a, the most recent estimation of the duration of the C3 segment is 230 kyr, based on the age model proposed by Martínez-Rodríguez et al. (2024). Thus, studies focused on the onset of OAE 1a (onset of C3 isotope segment) require a higher-resolution (millennial) scale. Notably, in this work, we have obtained a $\delta^{13}C$ curve at a higher resolution (i.e., 1 sample/ 0.242 kyr at the very onset of the CIE, and 1 sample/ 3 kyr for the rest of the interval) compared to other high-resolution records worldwide (e.g., 1 sample/ 3.61 kyr in Cismon section (Italy), or 1 sample/ 6.67 kyr for the DSDP Site 463 drill core (Pacific Ocean)) (Table 2).

Previous similar analyses on the entire Carbonero section (isotope segments C2 to C7) performed by Castro et al. (2019) (Fig. 6A), but at a lower resolution, highlighted a complexity in the biotic and environmental response throughout the entire OAE 1a, already showing the time lag between these perturbations at the onset of the event. Interestingly, although initial phases of the Ontong-Java Plateau volcanic

Table 2

Comparison of sampling time spacing of the $\delta^{13}C$ data between the Carbonero section and previous age-calibrated records of the C3 interval worldwide.

Section	Space sampling		Sampling time interval
Carbonero section[*] (this work)	Very onset of the CIE	1 sample/ 2 cm	1 sample/ 0.242 kyr
	Rest of the interval	1 sample/ 25 cm	1 sample/ 3.027 kyr
Cau core (E Spain)[†] (Castro et al., 2021)	Very onset of the CIE	1 sample/ 1 cm	1 sample/ 0.432 kyr
	Rest of the interval	1 sample/ 10.5 cm	1 sample/ 4.22 kyr
Cismon section (Italy)[*] (Méhay et al., 2009)	1 sample/ 2.12 cm		1 sample/ 3.61 kyr
DSDP Site 463 (Pacific)[*] (Bottini et al., 2015)	1 sample/ 17 cm		1 sample/ 6.67 kyr
YSPD-4 (NE China)[§] (Sun et al., 2025)	1 sample/ 100 cm		1 sample/ 11 kyr
La Bédoule core (SE France)[†] (Lorenzen et al., 2013)	1 sample/ 1.24 m		1 sample/ 71 kyr

[*] Deep pelagic basin.

[†] Distal open platform/ intra-shelf basin (hemipelagic).

[§] Continental lacustrine record.

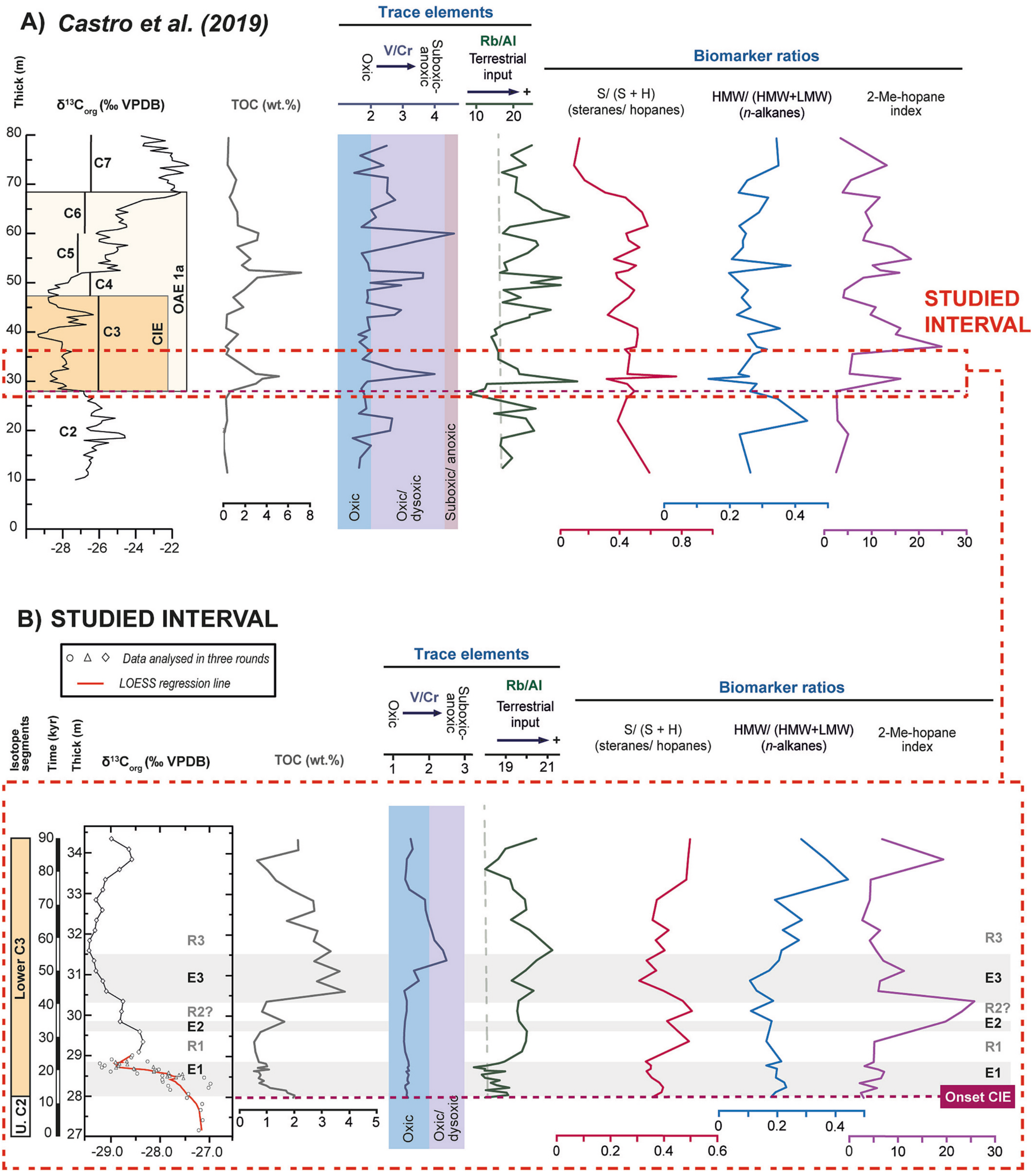

Fig. 6. Comparable resolution between the $\delta^{13}C_{org}$, TOC content and some elemental and biomarker proxies analysed in the entire Carbonero section performed by Castro et al. (2019) (A) and the studied interval in this work (B), which comprises the uppermost C2 to the lower C3 segments (ca. 80 kyr) at high resolution.

activity took place during the C2 segment (e.g., Bottini et al., 2012; Erba et al., 2015; Martínez-Rodríguez et al., 2021; Davidson et al., 2023; Matsumoto et al., 2024), apart from the nannoconid crisis event (Erba, 1994; Aguado et al., 1999), no significant biotic and environmental changes have been reported at this stage. Instead, the first important perturbations are recorded at the base of the C3 segment, i.e. associated with the onset of the negative C-isotope excursion (CIE) that initiates OAE 1a (Fig. 6A, B).

5.2. *Timing and expression of the environmental and biotic changes*

The analysis of the base of the C3 segment provided in this work allows the identification of three distinct successive negative carbon isotope excursions (E1 to E3) of different magnitude. Organic and inorganic proxies analysed here afford insights into the biotic and environmental changes associated to these CIEs, and their relative timing based on the age model provided by Martínez-Rodríguez et al. (2024).

The E1 interval (ca. 10 kyr) shows very little variation in productivity, continental input and redox proxies, with RSTEs suggesting deposition under well-oxygenated conditions (Fig. 4). Intriguingly, the S/(S + H) ratio that is expected to reflect algal vs bacteria productivity (e.g., Peters et al., 2005; Belin et al., 2018), is stable during E1 but increases as TOC decreases during R1 (Fig. 5), with this ratio indicating a major contribution of algae with respect to bacteria. The $C_{29}/(C_{27} + C_{28} + C_{29})$ sterane ratio, which can reflect the relative abundance of terrestrial (C_{29}) vs marine phytoplankton (C_{27}) and lacustrine algae (C_{28}) (Huang and Meinschein, 1979), or contribution of green (C_{28} and C_{29}) vs red algae (C_{27}) (Schwark and Empt, 2006), decreases during E1 and then sharply increases during the R1 recovery interval. Since the contribution of terrestrial input during R1 is relatively low, as indicated by the productivity P/Al proxy and continental (Rb/Al, K/Al, Zr/Al) ratios, it is probable that the $C_{29}/(C_{27} + C_{28} + C_{29})$ sterane ratio here reflects the relative contribution of algae groups (red vs green), rather than terrestrial input vs productivity. Several mechanisms have been proposed as controlling competition between green and red algae communities, such as nutrient availability, water salinity and redox conditions (Parker et al., 2008; Song et al., 2021; Chen et al., 2023). Green algae are more adaptable to oligotrophic conditions, whereas red algae flourish under mesotrophic-eutrophic settings (Parker et al., 2008). Green algae also show a greater salinity tolerance than red algae (Song et al., 2021), and can expand under oxygen-depleted conditions (Chen et al., 2023). Thus, changes in sterane distributions suggest a biotic response at the earliest stages of C3, likely mediated by environmental change. However, environmental variability appears to have been subtle, as the 2-MHI and HHI ratios show only minor variations in this interval, and RSTE values also remain notably stable through E1 up to R2 (Fig. 4).

During the second negative excursion (E2, 3 kyr) and its recovery interval (R2), elemental ratios exhibit very little change. Interestingly, E2 is associated with only a small increase in TOC contents and P/Al ratios, but an abrupt increase in S/(S + H) ratios and 2-MHIs (20 %), and a continued increase in $C_{29}/(C_{27} + C_{28} + C_{29})$, which suggests higher productivity (increased algae vs bacteria) and environmental change (i.e., possibly changes in the marine N-cycle, see discussion below), although waters maintained well-oxygenated conditions (RSTEs, HHI) (Figs. 4 and 5).

The E3 interval (ca. 15 kyr) started some 29 kyr after the onset of the CIE, and is associated with the most dramatic environmental and ecological changes in the section. This includes the initiation of sediment deposition under oxygen-depleted (anoxic) conditions, as indicated by the highest RSTE values and high HHIs (Figs. 4B and 5). The shift to more reducing conditions is coeval with an abrupt increase in TOC and P/Al productivity proxies, but a decrease in S/(S + H) ratios, as well as a subtle increase in terrigenous inputs (Rb/Al, K/Al). An associated decrease in the HMW/(HMW + LMW) *n*-alkane ratio, therefore, appears not to be associated with decreased terrestrial inputs but rather a change in algal assemblages. The decrease in S/(S + H) values also indicates a major contribution of bacteria compared to algae (e.g., Peters et al., 2005) at a time of anoxia development.

Interestingly, the 2-MHI decreases from 30 % at the onset of E3 to 5–10 % during this interval. This decoupling of anoxia from 2-MHIs in this section differs from previous studies (Kuypers et al., 2004; Ricci et al., 2017; Naafs et al., 2022). Oxygen-depleted (anoxic) conditions favour anaerobic microbial processes, including the reduction of nitrate and nitrite into N_2 (denitrification); this N loss could lead to the expansion of N_2-fixing cyanobacteria (Naafs et al., 2019, 2022). Thus, high 2-Me-hopane relative abundances associated with water column anoxia have been linked to an expansion of either N_2-fixing cyanobacteria (e.g., Kuypers et al., 2004), or more recently the spread of the denitrifier α-proteobacterium (Naafs et al., 2019, 2022). Regardless of the specific source, 2-MHIs appear to reflect the impact of anoxia on the marine N-cycle (Naafs et al., 2022; Jiang et al., 2025). The decoupling observed here suggests that E3 anoxia either a) did not bring about extensive detrinification in the water column; b) stimulated the growth of denitrifiers and/or N_2-fixing bacteria that do not produce 2-methylhopanes; or c) stimulated both 2-methylhopane producers but also non-methylated hopanoid-producing bacteria. The latter explanation is supported by the corresponding decrease in S/(S + H) ratios during the E3 interval, suggesting that E3 is characterized by a bloom of algae but also aerobic heterotrophic bacteria.

The E3 interval finishes with the negative C-isotope excursion that reaches the minimum values recorded here. TOC contents and most RSTEs persist from E3 values into R3 before returning gradually over 30 kyr to values similar to those at the base of the section. Biomarkers, however, show a different pattern in the latter part of R3 compared to the base of the section, characterized by gradual increase in S/(S + H) ratios, a decrease of $C_{29}/(C_{27} + C_{28} + C_{29})$ steranes, and a maximum in the HMW/(HMW + LMW) ratio, coinciding with deposition under well-oxygenated conditions as indicated by RSTEs and HHI proxies (Figs. 4 and 5). This variable pattern is the beginning of further changes in biomarker assemblages throughout OAE 1a previously reported by Castro et al., 2019 (see Section 5.1).

In summary, the variations obtained here in some of the biomarker ratios from the base of E1 (i.e., $C_{29}/(C_{27} + C_{28} + C_{29})$, 2-MHI, HHI) point to a very early response of the biotic system to the carbon cycle perturbation at the onset of OAE 1a, at the scale of thousands of years, although they become much more distinct during E2-E3. In contrast, the expansion of anoxia (RSTEs), coeval to primary productivity (P/Al, TOC), started some 29 kyr later (i.e., during E3 interval), and extended deep into R3 until eventually returning to pre-CIE values in the upper part of the section.

When considering the three CIEs together (E1-E3), there are some notable similarities and differences, documenting either distinct environmental or biotic local responses, or a complex interplay between regional and global signals. It is noteworthy that both E1 and E3 are each characterized by low S/(S + H) ratios. However, most of the other proxies document distinct responses to the CIEs. Most notably, TOC contents, all of the redox proxies and the P/Al productivity proxy, all exhibit a maximum associated with E3 that slowly recovers in R3, but they are all low and invariant in E1 and E2. This suggests a decoupling between biotic assemblages and organic matter productivity and burial. Potentially, the S/(S + H) ratio and other biomarker indicators are recording local biotic changes, whereas the RSTEs are recording regional or global changes. This assumption, however, needs further studies at a similar high-resolution to potentially discern the global vs local/regional character of both the biotic and environmental changes described.

Our high-resolution study provides a detailed insight into the first ca. 80 kyr after the onset of OAE 1a. These results reveal the existence of three carbon isotope excursions, i.e. E1 to E3, which are associated with different biotic and environmental changes. While initial stress conditions at the very onset of OAE 1a triggered an early biotic response (E1-E2), the most dramatic changes and the development of major anoxia occurred some 29 kyr later (E3), similar to the delay estimated from the pelagic Cismon basin (ca. < 30 kyr, Bauer et al., 2021), although based on different age models. Such differences open the discussion about the mechanisms behind the E1-E3 carbon isotope excursions, which represent the beginning of a prolonged period (ca. 1.4 Myr) of biotic and environmental instability during OAE 1a.

5.3. Relative roles of CO_2 volcanic degassing and methane emissions at the onset of OAE 1a

Submarine Large Igneous Province (LIP) volcanic activity has been widely accepted to be the primary triggering mechanism of the environmental perturbations related to OAE 1a. However, the origin of the volcanism is debated (role of different LIPs), with some suggesting the High Artic Large Igneous Province (HALIP) (Davidson et al., 2023) as the main volcanic source instead of the traditionally invoked Ontong-Java Plateau (OJP) volcanism in the central Pacific Ocean (e.g., Erba, 1994; Jones and Jenkyns, 2001; Tejada et al., 2009; Bottini et al., 2012; Erba et al., 2015; Percival et al., 2021; Bauer et al., 2024). Nevertheless, recent radiometric dating performed by Matsumoto et al. (2024) has unambiguously linked the OJP volcanism as the major driver of this carbon cycle perturbation. On the other hand, methane emissions have been also invoked to play a key role in the onset of OAE 1a (e.g., Méhay et al., 2009; Erba et al., 2010; Bottini et al., 2015; Adloff et al., 2020). These two explanations are compatible, and even linked with each other regarding the triggering mechanism, as the rise in pCO_2 related to the OJP volcanism and subsequent global warming can result in destabilization of deposits of methane, resulting in massive emissions to the atmosphere (e.g., Jahren et al., 2005; Méhay et al., 2009; Adloff et al., 2020). Additionally, sill intrusions into organic-rich sediments during the early Aptian could cause the release of thermogenic and/or biogenic methane (Polteau et al., 2016; Bauer et al., 2017; Adloff et al., 2020; Percival et al., 2025).

The high-resolution C-isotope stratigraphy provided in this work allows us to identify three negative C-isotope shifts at the very onset of OAE 1a in the Carbonero section, i.e., the E1 to E3 intervals (Fig. 7A). Interestingly, these carbon isotope excursions are of variable magnitude, with implications for their respective origins. A recent high-resolution reconstruction of the C-isotope stratigraphy and Ontong-Java volcanic activity from a hemipelagic section in the Western Tethys (Cau core, Fig. 7B) (Martínez-Rodríguez et al., 2021), allows us to compare and hypothesize about the origin of these C-isotope excursions. In the Cau section, an early phase of the OJP volcanic activity, predating the onset of the CIE (i.e., during C2 segment) (Fig. 7B), is recorded by increased $^{187}Os/^{188}Os$ (radiogenic) values punctuated by mantle-derived (OJP) depleted unradiogenic $^{187}Os/^{188}Os$ ratios (e.g., Peucker-Ehrenbrink and Ravizza, 2000; Tejada et al., 2009), similar to records from other sections from the Tethys and Pacific Oceans (Méhay et al., 2009; Tejada et al., 2009; Erba et al., 2010; Bottini et al., 2012, 2015). However, in the Cau core, the onset of the CIE, which is also recognized by a pronounced negative C-isotope excursion of similar magnitude and time duration as in Carbonero section (E1 interval), is not accompanied by decreased mantle-derived $^{187}Os/^{188}Os$ ratios. An increase in weathering could also account for a change in Os-isotope records (e.g., Lechler et al., 2015; Percival et al., 2021).

Alternatively, additional carbon cycle perturbation could have co-occurred or been caused by the volcanic CO_2 emissions, contributing to the pronounced and rapid negative C-isotope excursions at the onset of OAE 1a. In this regard, the Carbonero C-isotope profile shows a stepped negative pattern within the C-isotope excursion E1, with a marked increase in the slope in E1b that occurs 6 kyr after the onset of OAE 1a, with a duration of ca. 4 kyr (Fig. 7A). Based on the magnitude and short-time character of this conspicuous spike, and the Cau core Os-isotope record by Martínez-Rodríguez et al. (2021) (Fig. 7B), we suggest that this change could be explained by methane (CH_4) emissions at a

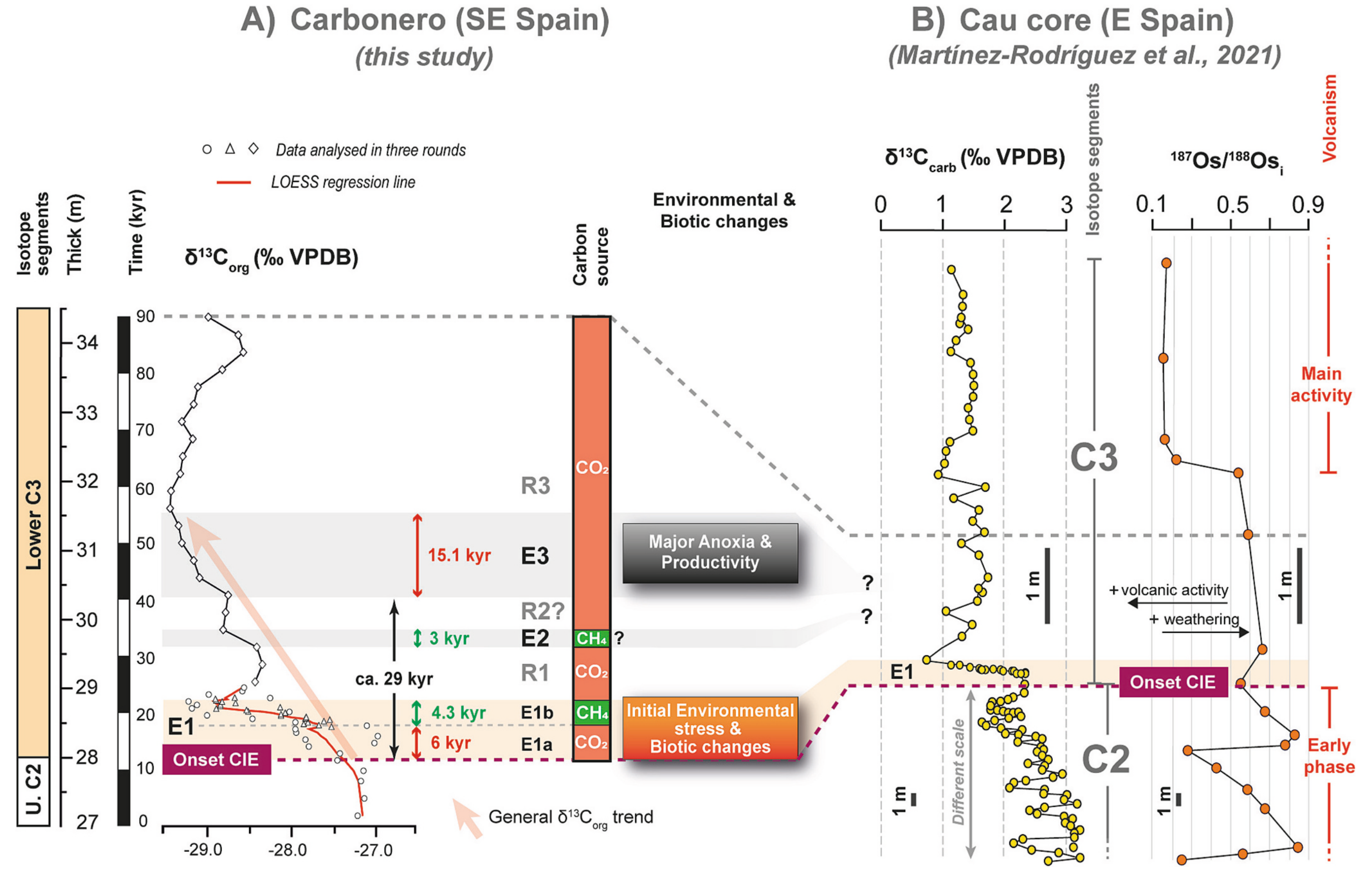

Fig. 7. (A) Time estimations (kyr) for the key episodes at the studied interval, and carbon sources for ^{13}C-depleted carbon (CO_2 and CH_4) (see text for discussion). (B) Record of volcanic activity in the Western Tethys (Cau core, E Spain) through Os-isotope variations (Martínez-Rodríguez et al., 2021), and the $\delta^{13}C_{carb}$ profile (note the different scales for C2 and C3 segments). The E1 C-isotope excursion identified in the studied section is also recorded in the Cau $\delta^{13}C_{carb}$ profile.

global scale (i.e., destabilization of seafloor methane deposits (melting of methane hydrates) due to increased bottom water temperatures). These emissions could be a consequence of the warming derived from volcanic CO_2 degassing during the early phase of the OJP volcanic activity and the E1a interval, and/or sill intrusions into organic-rich sediments (e.g., Jahren et al., 2005; Méhay et al., 2009; Erba et al., 2010; Polteau et al., 2016; Adloff et al., 2020; Percival et al., 2025). An additional local CH_4 release from biotic methanogenesis cannot be discounted in Carbonero, and will be explored in future studies.

Methane release, due to methane's low $\delta^{13}C$ values, can drive rapid and larger C-isotope shifts than similar carbon emissions from volcanic processes (e.g., Wagner et al., 2007; Bauer et al., 2017; Huang et al., 2024). Although methane has a higher global warming potential, it is rapidly converted to CO_2 in the atmosphere (e.g., Balcombe et al., 2018). Therefore, the climate perturbation for a given shift in $\delta^{13}C$ caused by methane is generally smaller than for the same C-isotope shift caused by volcanic emissions (e.g., Pagani et al., 2006). This could explain why the marked C-isotope shift of the E1b interval appears to have minimal environmental impacts in the Carbonero section, reflected only by changes in biomarker assemblages (mainly steranes and hopanes; Figs. 4–5 and 7). The second, less pronounced excursion, the E2 interval (3 kyr), is also characterized by minor environmental change and might also represent a methane pulse, although weaker than E1b (Fig. 7). After this initial phase, continuous less ^{13}C-depleted volcanic emissions from the Ontong-Java Plateau activity could have driven the E3 C-isotope excursion, and it is during this time that minimum $\delta^{13}C_{org}$ values are reached. Consequently, it is only during E3 that major environmental changes occurred, with the development of pronounced anoxia and enhanced productivity together with biotic changes (Fig. 8).

This double-source for ^{13}C-depleted carbon at the onset of OAE 1a as

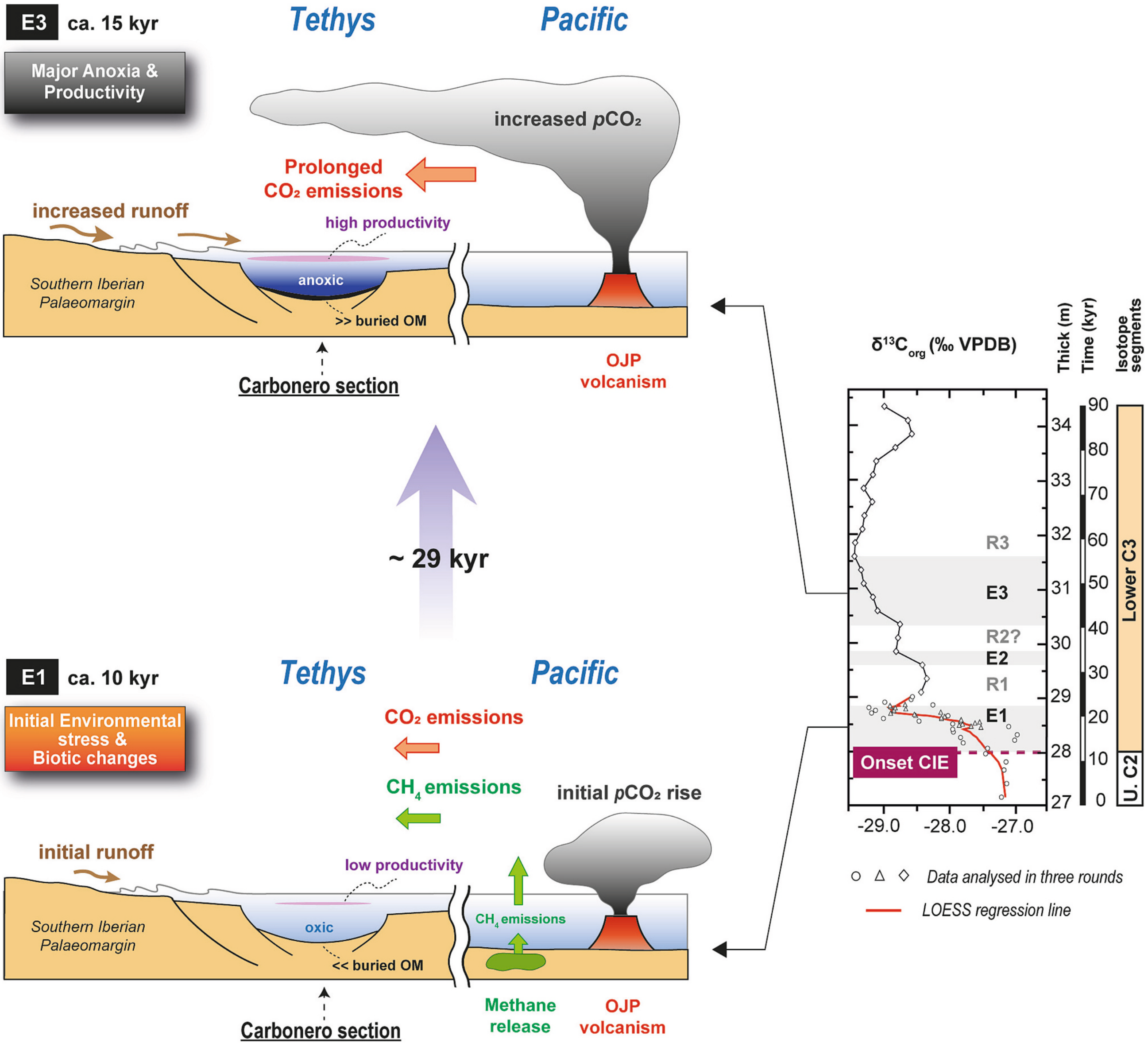

Fig. 8. Schematic representation of the factors controlling the biotic and environmental changes in E1 and E3 intervals (see text for discussion). During E1 interval (time duration of ca. 10 kyr), a probable global methane release occurred, probably driven by the global warming caused by initial volcanic CO_2 emissions from the OJP activity (Pacific Ocean) and/or sill intrusions into organic-rich sediments, which conducted the marked negative C-isotope shift that characterizes the E1 excursion. During this interval, the Carbonero section (Tethys Ocean) did not record significant environmental changes, documenting well-oxygenated (oxic) conditions but a rapid impact on biological systems (initial environmental stress and biotic changes) in this part of the Southern Iberian Palaeomargin. The major anoxia development instead took place some 29 kyr after the onset of the negative CIE, during the E3 interval (ca. 15 kyr), with increased runoff and productivity, and higher organic matter (OM) accumulation, after prolonged CO_2 emissions (increased atmospheric $pCO2$ concentrations).

theorised here agrees with previous hypotheses based on climate models (Adloff et al., 2020), and the C- and Os-isotope records from the Tethys and Pacific Oceans (e.g., Cismon core, Gorgo a Cerbara section and DSDP site 463 drill core; Méhay et al., 2009; Bottini et al., 2012, 2015) (Fig. 9A). These previous interpretations (Adloff et al., 2020) highlighted that a predominant input from an isotopically light carbon source such as methane (with $\delta^{13}C < -40$ ‰) was necessary to drive the CIE at the onset of OAE 1a. Similar hypotheses were also proposed by Van Breugel et al. (2007) and Méhay et al. (2009) in Cismon section (Italy). More recently, Bauer et al. (2022) in both Cismon and DSDP Site 463 core also suggested that methane release could occur under low seawater sulphate concentrations. Moreover, Percival et al. (2025) reported a clear intensification of the OJP volcanism during the upper C3-lower C4 segments, based on Os-isotopes, Hg content and TEX_{86} paleotemperature data in several sections worldwide.

This does not preclude a role for volcanism at the onset of OAE 1a. Bauer et al. (2021) identified three short-lived volcanic pulses, i.e. at the upper C2, and at the transition of C2-C3 and C3-C4 segments (pulses 1 to 3 in Fig. 9A), by analysing the Eu, Mn and Cr-isotope data from the DSDP Site 463 drill core in the Pacific Ocean. Even if assuming that the first OJP pulse (pulse 1) reported by Bauer et al. (2021) coincided with the punctuated decreased $^{187}Os/^{188}Os$ (mantle-derived) values reported in the upper C2 segment of the Cau core, and the second OJP pulse (pulse 2) at the C2-C3 transition coincides with the E1a interval of the Carbonero section (Figs. 7B and 9A), the duration of this intensified OJP phase could not itself explain the magnitude of the negative C-isotope excursion represented in the E1b interval.

Future work, therefore, should focus on ascertaining the global significance of the Carbonero sharp negative C-isotope excursion E1b. Noteworthily, it is not recorded in the $\delta^{13}C$ curve of the DSDP Site 463 core (Pacific Ocean) (Bottini et al., 2015), or even in the high-resolution $\delta^{13}C$ record obtained by Méhay et al. (2009) in Cismon (Itay) (Fig. 10), with the latter evidencing a long-term negative $\delta^{13}C$ trend at the base of C3 segment that could represent the entire E1-E3 interval in the Carbonero section (Fig. 9). In fact, apart from the Carbonero site, this sharp negative C-isotope shift at the very onset of OAE 1a is only observed in those sections with an expanded record of the event (e.g., Cau core, El Pui and Mount Pagasarri sections in Spain; Castro et al. (2021), Sanchez-Hernandez and Maurrasse (2016) and Fernández-Mendiola et al. (2018), respectively), as shown in Fig. 10. Its absence elsewhere can be explained by either the resolution of the sampling, the lesser completeness of the OAE 1a record, or both.

Our study provides new insights into the biotic and environmental changes associated with the very onset of OAE 1a. The only available record at a similar high-resolution scale for comparing both the C-isotope record and the biotic and environmental changes associated is that provided by Méhay et al. (2009) in Cismon (Italy), who performed a detailed study of the lower part of the C3 segment in this section (Fig. 9A). These authors also concluded the existence of initial phases of volcanogenic CO_2 degassing prior to the CH_4 release, which coincides with an increase in productivity as revealed by the C-isotope signature of specific *n*-alkanes (interval IV in Méhay et al., 2009) (Fig. 9A). These authors divided the lower part of the C3 segment in five intervals (I to V), marked by changes in both organic ($\delta^{13}C_{n\text{-alkanes}}$) and inorganic ($\delta^{13}C_{carb}$) isotope records. The first evidence of some perturbation in marine organisms is reported at around 30 kyr after the onset of the CIE, recording a positive $\delta^{13}C$ shift in biomarkers that these authors relate to changes in both terrestrial and marine (algae) productivity. In

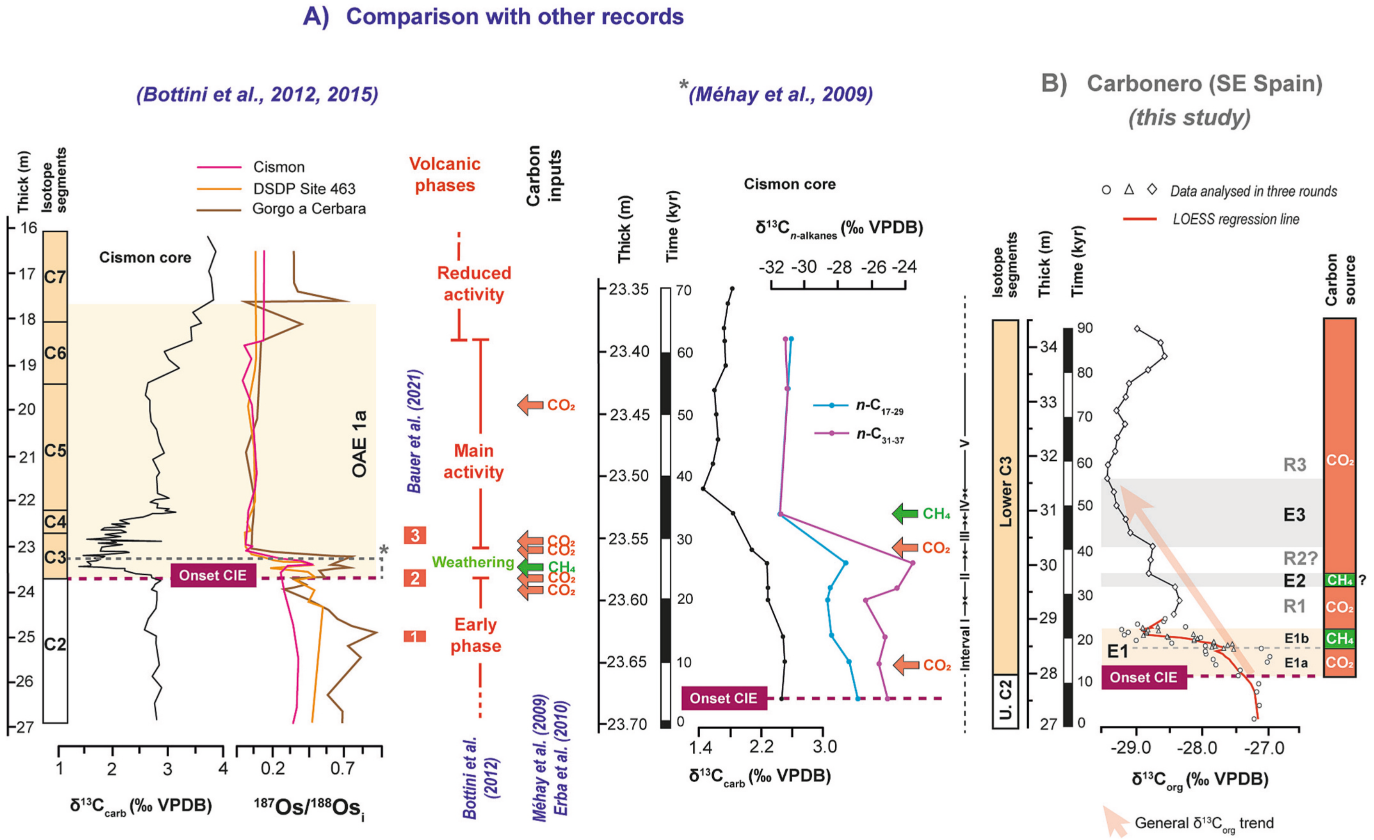

Fig. 9. Comparison between the C-isotope stratigraphy, Os-isotope data and interpreted carbon sources from several records in the Tethyan (Cismon core, Gorgo a Cerbara) and Pacific (DSDP Site 463) Oceans (A), with the C-isotope stratigraphy and interpreted carbon sources in Carbonero section (this study) (B). Volcanism and carbon sources data shown in (A) are taken from Bottini et al. (2012) and Bauer et al. (2021; pulses 1–3) for volcanism, and from Méhay et al. (2009) and Erba et al. (2010) for CO_2 and CH_4 pulses. The interval corresponding to the data shown by Méhay et al. (2009) represents a more detailed analysis of the onset of OAE 1a at Cismon core (dash rectangle marked with an asterisk), including the $\delta^{13}C_{carb}$ stratigraphy, biomarker (*n*-alkanes) data and interpreted CO_2 and CH_4 pulses.

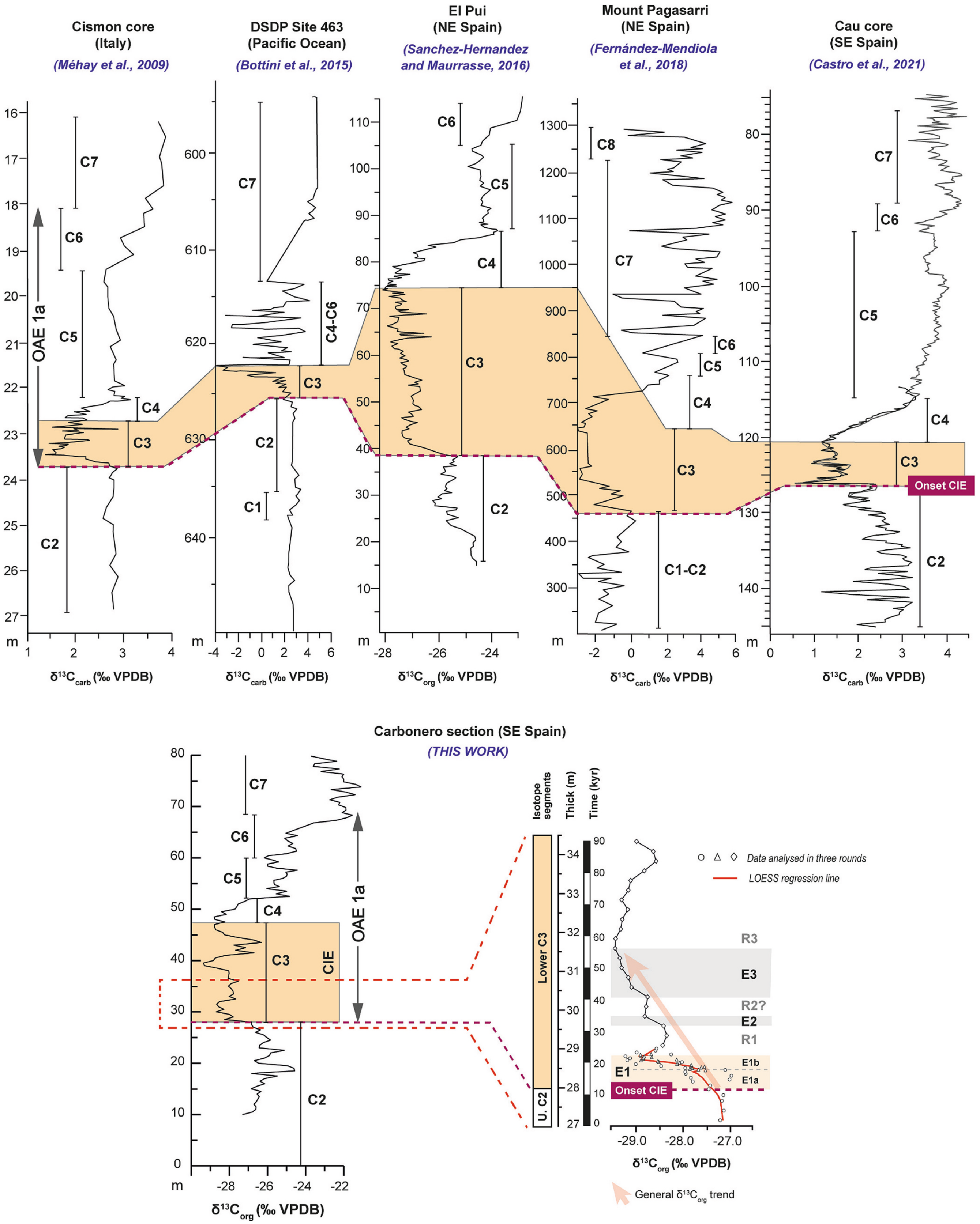

Fig. 10. Comparison of the C3 C-isotope stratigraphy between the Cismon (Italy) (Méhay et al., 2009) and DSDP Site 463 (Pacific Ocean) (Bottini et al., 2015) cores, and expanded records of the OAE 1a (El Pui, Mount Pagasarri and Cau in Spain; Sanchez-Hernandez and Maurrasse, 2016; Fernández-Mendiola et al., 2018; Castro et al., 2021, respectively), with the C3 C-isotope stratigraphy for the Carbonero section (this work). The sharp negative C-isotope shift E1b that is revealed in the Carbonero section, is only observed in those sections with an expanded record of the OAE 1a (i.e., Cau, Mount Pagasarri and El Pui) (see text for discussion).

Carbonero, biomarker data suggest that changes in biota already occurred at the very onset of the CIE (E1 interval), and major anoxia and productivity took place some 29 kyr after the onset (E3 interval) (Fig. 8). In addition, based on the age model used by Méhay et al. (2009), the methane pulse that originated the major shift in the C-isotope curve would occur some 30 kyr after the onset of OAE 1a (onset of the CIE). In contrast, the Carbonero C-isotope curve obtained here reveals that the CH_4 pulse would take place only 6 kyr after the onset of OAE 1a (E1b excursion), and possibly a second pulse at ca. 20 kyr (E2; Fig. 9B).

6. Conclusions

The new high-resolution study of the very onset of OAE 1a presented here clearly demonstrates that the beginning of the carbon cycle perturbation had a rapid impact on biological systems over a timescale of several kyrs. This first response affected the balance of algae and bacteria, and could reflect the first of several OAE 1a perturbations in the marine nitrogen cycle. Crucially, the development of anoxia and an increase in primary productivity took place some 29 kyr after the onset of OAE 1a. The entire OAE 1a onset interval is characterized by the widely recognized negative carbon isotopic excursion in the ocean-atmosphere reservoir, but the stratigraphic resolution has revealed at least three negative CIEs (E1 to E3) within the longer-term trend. The long-term shift is likely due to volcanic degassing from the Ontong-Java Plateau volcanism, whereas particularly the first C-isotope spike (E1b) could reflect a pulse of methane release, possibly triggered by the early stages of volcanism and/or sill intrusions into organic-rich sediments. Thus, the CIEs do not represent equivalent CO_2 release events; instead, most CO_2 change likely occurred during the final CIE E3, which could explain why it is associated with the most dramatic environmental change. This study over an interval of ca. 80 kyr provides a novel perspective into the OAE 1a, revealing both long-term (10s of kyrs) and extremely rapid (kyrs) carbon isotopic shifts. Our results highlight the importance of in-depth studies of this and similar hyperthermal events for the understanding of the recover adaptability of the Earth system to global carbon cycle perturbations at a short-time (few thousands of years) scale.

CRediT authorship contribution statement

Cristina Sequero: Writing – review & editing, Writing – original draft, Methodology, Investigation, Formal analysis, Data curation, Conceptualization. **Sandro Froehner:** Validation, Methodology, Data curation. **José Manuel Castro:** Writing – review & editing, Supervision, Project administration, Funding acquisition, Formal analysis, Conceptualization, Investigation. **Ginés A. De Gea:** Writing – review & editing, Methodology, Investigation, Funding acquisition, Conceptualization. **María Luisa Quijano:** Writing – review & editing, Methodology, Investigation. **B. David A. Naafs:** Writing – review & editing, Investigation. **Richard D. Pancost:** Writing – review & editing, Investigation, Conceptualization.

Declaration of competing interest

The authors declare the following financial interests/personal relationships which may be considered as potential competing interests:

Jose Manuel Castro reports financial support was provided by Junta de Andalucía Consejería de Economía y Conocimiento. Cristina Sequero reports financial support was provided by Junta de Andalucía Consejería de Economía y Conocimiento. Jose Manuel Castro reports financial support was provided by Spain Ministry of Science and Innovation. Sandro Froehner reports financial support was provided by Capes Print. If there are other authors, they declare that they have no known competing financial interests or personal relationships that could have appeared to influence the work reported in this paper.

Acknowledgments

Authors want to express their acknowledgement and recognition to our late colleague Roque Aguado, who participated in the initiation of this investigation, and served as an inspiration to the research group over the last decades. This study was funded by the Research Projects P20_00783 (Junta de Andalucía, Consejería de Economía y Conocimiento, Spain), FEDER-UJA 1265149 (Junta de Andalucía, Consejería de Economía y Conocimiento, Spain), PID2023-151264NB-I00 (Spanish Government) and the Research Group RNM-200 (Junta de Andalucía, Consejería de Economía y Conocimiento, Spain). SF thanks to Capes/Print (88887.582251/2020-00) (Brazil). Authors would also like to acknowledge to the two anonymous reviewers and to the editorial work done by Dr. Maoyan Zhu, who have contributed to significantly improve the final version of the manuscript.

Appendix A. Supplementary data

Supplementary data to this article can be found online at https://doi.org/10.1016/j.gloplacha.2025.105170.

Data availability

The research data are included in the Supplementary Material

References

Adloff, M., Greene, S.E., Parkinson, I.J., Naafs, B.D.A., Preston, W., Ridgwell, A., Lunt, D. J., Castro, J.M., Monteiro, F.M., 2020. Unravelling the sources of carbon emissions at the onset of Oceanic Anoxic Event (OAE) 1a. Earth Planet. Sci. Lett. 530, 115947. https://doi.org/10.1016/j.epsl.2019.115947.

Aguado, R., Molina, J.M., O'Dogherty, L., 1993. Bioestratigrafía y litoestratigrafía de la Formación Carbonero (Barremiense-Albiense?) en la transición Subbético Externo–Subbético Medio (Sur de Jaén). Cuad. Geol. Ibér. 17, 325–344.

Aguado, R., Castro, J.M., de Gea, G.A., 1999. Aptian bioevents – an integrated biostratigraphic analysis of the Almadich Formation, Inner Prebetic Domain, SE Spain. Cretac. Res. 20, 663–683.

Aguado, R., de Gea, G.A., Castro, J.M., O'Dogherty, L., Quijano, M.L., Naafs, B.D.A., Pancost, R.D., 2014. Late Barremian–early Aptian dark facies of the Subbetic (Betic Cordillera, southern Spain): Calcareous nannofossil quantitative analyses, chemostratigraphy and palaeoceanographic reconstructions. Palaeogeogr. Palaeoclimatol. Palaeoecol. 395, 198–221. https://doi.org/10.1016/j.palaeo.2013.12.031.

Balcombe, P., Speirs, J.F., Brandon, N.P., Hawkes, A.D., 2018. Methane emissions: choosing the right climate metric and time horizon. Environ Sci Process Impacts 20 (10), 1323–1339. https://doi.org/10.1039/C8EM00414E.

Bauer, K.W., Zeebe, R.E., Wortmann, U.G., 2017. Quantifying the volcanic emissions which triggered Oceanic Anoxic Event 1a and their effect on ocean acidification. Sedimentol 64, 204–214. https://doi.org/10.1111/sed.12335.

Bauer, K.W., Bottini, C., Frei, R., Asael, D., Planavsky, N.J., Francois, R., McKenzie, N.R., Erba, E., Crowe, S.A., 2021. Pulsed volcanism and rapid oceanic deoxygenation during Oceanic Anoxic Event 1a. Geology 49, 1452–1456. https://doi.org/10.1130/G49065.1.

Bauer, K.W., Bottini, C., Katsev, S., Jellinek, M., Francois, R., Erba, E., Crowe, S.A., 2022. Ferruginous oceans during OAE1a and collapse of the marine sulfate pool. Earth Planet. Sci. Lett. 578, 117324. https://doi.org/10.1016/j.epsl.2021.117324.

Bauer, K.W., McKenzie, N.R., Cheung, C.T.L., Gambacorta, G., Bottini, C., Nordsvan, A. R., Erba, E., Crowe, S.A., 2024. A climate threshold for ocean deoxygenation during the early cretaceous. Nature 633, 582–586. https://doi.org/10.1038/s41586-024-07876-1.

Beerling, D.J., Royer, D.L., 2002. Fossil plants as indicators of the Phanerozoic Global Carbon Cycle. Annu. Rev. Earth Planet. Sci. 30, 527–556. https://doi.org/10.1146/annurev.earth.30.091201.141413.

Beil, S., Kuhnt, W., Holbourn, A., Scholz, F., Oxmann, J., Wallmann, K., Lorenzen, J., Aquit, M., Hassane Chellai, E., 2020. Cretaceous oceanic anoxic events prolonged by phosphorus cycle feedbacks. Clim. Past 16 (2), 757–782. https://doi.org/10.5194/CP-16-757-2020.

Belin, B.J., Busset, N., Giraud, E., Molinaro, A., Silipo, A., Newman, D.K., 2018. Hopanoid lipids: from membranes to plant-bacteria interactions. Nat. Rev. Microbiol. 16 (5), 304–315. https://doi.org/10.1038/nrmicro.2017.173.

Bishop, N., Farrimond, P., 1995. A new method of comparing extended hopane distributions. Org. Geochem. 23 (10), 987–990. https://doi.org/10.1016/0146-6380(95)00074-7.

Bodin, S., Godet, A., Matera, V., Steinmann, P., Vermeulen, J., Gardin, S., Adatte, T., Coccioni, R., Föllmi, K.B., 2007. Enrichment of redox-sensitive trace metals (U, V, Mo, As) associated with the late Hauterivian Faraoni oceanic anoxic event. Int. J. Earth Sci. 96 (2), 327–341. https://doi.org/10.1007/s00531-006-0091-9.

Bottini, C., Cohen, A.S., Erba, E., Jenkyns, H.C., Coe, A.L., 2012. Osmium isotope evidence for volcanism, weathering and ocean mixing during the early Aptian OAE 1a. Geology 40, 583–586. https://doi.org/10.1130/G33140.1.

Bottini, C., Erba, E., Tiraboschi, D., Jenkyns, H.C., Schouten, S., Sinninghe Damsté, J.S., 2015. Climate variability and ocean fertility during the Aptian stage. Clim. Past 11 (3), 383–402. https://doi.org/10.5194/cp-11-383-2015.

Bralower, T.J., Leckie, R.M., Sliter, W.V., Thierstein, H.R., 1995. An integrated cretaceous microfossil biostratigraphy. SEPM Spec. Publ. 65–79.

Brumsack, H.J., 2006. The trace metal content of recent organic carbon-rich sediments: implications for cretaceous black shale formation. Palaeogeogr. Palaeoclimatol. Palaeoecol. 232, 344–361. https://doi.org/10.1016/j.palaeo.2005.05.011.

Calvert, S.E., Pedersen, T.F., 2007. Chapter fourteen-elemental proxies for palaeoclimatic and palaeoceanographic variability in marine sediments: interpretation and application. In: Hillaire-Marcel, C., De Vernal, A. (Eds.), Developments in Marine Geology, 1. ElSevier, pp. 567–644. https://doi.org/10.1016/S1572-5480(07)01019-6.

Castro, J.M., de Gea, G.A., Quijano, M.L., Aguado, R., Froehner, S., Naafs, B.D.A., Pancost, R.D., 2019. Complex and protracted environmental and ecological perturbations during OAE 1a - evidence from an expanded pelagic section from South Spain (Western Tethys). Glob. Planet. Chang. 183, 103030. https://doi.org/10.1016/j.gloplacha.2019.103030.

Castro, J.M., Ruiz-Ortiz, P.A., de Gea, G., Aguado, R., Jarvis, I., Weissert, H., Molina, J. M., Nieto, L.M., Pancost, R.D., Quijano, M.L., Reolid, M., Skelton, P.W., López-Rodríguez, C., Martínez-Rodríguez, R., 2021. High-resolution C-isotope, TOC and biostratigraphic records of OAE 1a (Aptian) from an expanded hemipelagic cored succession, western Tethys: a new stratigraphic reference for global correlation and paleoenvironmental reconstruction. Paleoceanogr. Paleoclimatol. 36 (3), e2020PA004004. https://doi.org/10.1029/2020PA004004.

Castro, J.M., Sequero, C., Quijano, M.L., de Gea, G.A., Naafs, B.D.A., Pancost, R.D., 2025. Influence of local factors con the expression of the early Aptian OAE 1a – insights from a pelagic basin in the Western Tethys. Palaeogeogr. Palaeoclimatol. Palaeoecol. 676, 113167. https://doi.org/10.1016/j.palaeo.2025.113167.

Charbonnier, G., Boulila, S., Spangenberg, J.E., Vermeulen, J., Galbrun, B., 2023. Astrochronology of the Aptian stage and evidence for the chaotic orbital motion of Mercury. Earth Planet. Sci. Lett. 610, 118104. https://doi.org/10.1016/J.EPSL.2023.118104.

Chen, J., Hogancamp, N., Lu, M., Ikejiri, T., Malina, N., Ojeda, A., Sun, Y., Lu, Y., 2023. Lipid biomarkers recording marine microbial community structure changes through the Frasnian- Famennian mass extinction event. Geobiology 21 (6), 725–742. https://doi.org/10.1111/gbi.12568.

Chumakov, N.M., Zharkov, M.A., Herman, A.B., Doludenko, M.P., Kalandadze, N.N., Lebedev, E.L., Ponomarenko, A.G., Rautian, A.S., 1995. Climatic belts of the mid-cretaceous time. Stratigr. Geol. Correl. 3 (3), 42–63.

Cleveland, W.S., Devlin, S.J., 1988. Locally weighted regression: an approach to regression analysis by local fitting. J. Am. Stat. Assoc. 83, 596–610.

Davidson, P.C., Koppers, A.A.P., Sano, T., Hanyu, T., 2023. A younger and protracted emplacement of the Ontong Java Plateau. Science 380, 1185–1188. https://doi.org/10.1126/science.ade8666.

de Gea, G.A., 2004. Bioestratigrafía y eventos del Cretácico Inferior en las Zonas Externas de la Cordillera Bética [Ph.D. thesis]. University of Jaén, Jaén, p. 658.

de Gea, G.A., Aguado, R., Castro, J.M., Molina, J.M., O'Dogherty, L., Ruiz Ortiz, P.A., 2008a. Lower Aptian Subbetic organic-rich facies. Radiolarites and associated deposits: the local expression of Oceanic Anoxic Event 1a (Carbonero Formation. Southern Spain). Cretac. Res. 29, 861–870. https://doi.org/10.1016/j.cretres.2008.05.011.

de Gea, G.A., Aguado, R., Castro, J.M., Molina, J.M., Ruiz Ortiz, P.A., 2008b. Registro del evento anóxico del Aptiense inferior en la cuenca subbética (Sur de Jaén): La Formación Carbonero. Geotemas 10, 135–138.

Eglinton, G., Hamilton, R.J., 1967. Leaf epicuticular waxes. Science 156, 1322–1335. https://doi.org/10.1126/science.156.3780.1322.

Erba, E., 1994. Nannofossils and superplumes: the early Aptian 'nannoconid crisis'. Paleoceanography 9, 483–501. https://doi.org/10.1029/94PA00258.

Erba, E., 2004. Calcareous nannofossils and Mesozoic Oceanic Anoxic events. Mar. Micropaleontol. 52, 85–106.

Erba, E., Bottini, C., Weissert, H.J., Keller, C.E., 2010. Calcareous nannoplankton response to surface-water acidification around Oceanic Anoxic Event 1a. Science 329, 428–432. https://doi.org/10.1126/science.1188886.

Erba, E., Duncan, R.A., Bottini, C., Tiraboschi, D., Weissert, H., Jenkyns, H.C., Malinverno, A., 2015. Environmental consequences of Ontong Java Plateau and Kerguelen Plateau volcanism. In: Neal, C.R., Sager, W.W., Sano, T., Erba, E. (Eds.), The Origin, Evolution, and Environmental Impact of Oceanic Large Igneous Provinces. Geol. Soc. Am. Spec. Pap, 511, pp. 271–303. https://doi.org/10.1130/2015.2511(15).

Fernández-Mendiola, P.A., Mendicoa, J., Owen, H.G., García-Mondéjar, J., 2018. The early Aptian (cretaceous) stratigraphy of Mount Pagasarri (N Spain): Oceanic anoxic event-1a. Geol. J. 53 (5), 1802–1822. https://doi.org/10.1002/gj.3008.

Gradstein, F.M., Ogg, J.G., Schmitz, M.D., Ogg, G.M., 2020. The Geologic Time Scale 2020. Elsevier, Amsterdam, p. 1144. https://doi.org/10.1016/C2020-1-02369-3.

Hay, W.W., 2017. Toward understanding cretaceous climate—an updated review. Sci. China Earth Sci. 60, 5–19. https://doi.org/10.1007/s11430-016-0095-9.

Huang, W.Y., Meinschein, W.G., 1979. Sterols as ecological indicators. Geochim. Cosmochim. Acta 43, 739–745. https://doi.org/10.1016/0016-7037(79)90257-6.

Huang, Y., Jin, X., Pancost, R.D., Kemp, D.B., Naafs, B.D.A., 2024. An intensified lacustrine methane cycle during the Toarcian OAE (Jenkyns Event) in the Ordos Basin, northern China. Earth Planet. Sci. Lett. 639, 118766. https://doi.org/10.1016/j.epsl.2024.118766.

Huck, S., Rameil, N., Korbar, T., Heimhofer, U., Wieczorek, T.D., Immenhauser, A., 2010. Latitudinally different responses of Tethyan shoal-water carbonate systems to the early Aptian Oceanic Anoxic Event (OAE 1a). Sedimentology 57, 1585–1614. https://doi.org/10.1111/j.1365-3091.2010.01157.x.

Huck, S., Heimhofer, U., Rameil, N., Bodin, S., Immenhauser, A., 2011. Strontium and carbon-isotope chronostratigraphy of Barremian–Aptian shoal-water carbonates: Northern Tethyan platform drowning predates OAE 1a. Earth Planet. Sci. Lett. 304, 547–558. https://doi.org/10.1016/j.epsl.2011.02.031.

Immenhauser, A., Hillgärtner, H., van Bentum, E., 2005. Microbial-foraminiferal episodes in the early Aptian of the southern Tethyan margin: Ecological significance and possible relation to Oceanic Anoxic Event 1a. Sedimentology 52, 77–99. https://doi.org/10.1111/j.1365-3091.2004.00683.x.

Jacoby, W.G., 2000. Loess: a nonparametric, graphical tool for depicting relationships between variables. Elect. Stud. 19, 577–613. https://doi.org/10.1016/S0261-3794(99)00028-1.

Jahren, A.H., Conrad, C.P., Crystal Arens, N., Mora, G., Lithgow-Bertelloni, C., 2005. A plate tectonic mechanism for methane hydrate release along subduction zones. Earth Planet. Sci. Lett. 236, 691–704. https://doi.org/10.1016/j.epsl.2005.06.009.

Jenkyns, H.C., 2010. Geochemistry of oceanic anoxic events. Geochem. Geophys. Geosyst. 11 (3). https://doi.org/10.1029/2009GC002788.

Jenkyns, H.C., 2018. Transient cooling episodes during cretaceous Oceanic Anoxic events with special reference to OAE 1a (early Aptian). Philos. Trans. R. Soc. A 376, 20170073. https://doi.org/10.1098/rsta.2017.0073.

Jiang, S., Cui, Y., Wang, Y., De Palma, M., Naafs, B.D.A., Jiang, J., Hu, X., Wu, H., Chu, R., Gu, Y., Wang, J., Huang, Y., Ingalls, M., Bralower, T.J., Yang, S., Zachos, J. C., Ridgwell, A., 2025. Millennial-timescale thermogenic CO_2 release preceding the Paleocene-Eocene thermal Maximum. Nat. Commun. 16 (1), 1–12. https://doi.org/10.1038/s41467-025-60939-3.

Jones, C.E., Jenkyns, H.C., 2001. Seawater strontium isotopes, Oceanic Anoxic events, and seafloor hydrothermal activity in the Jurassic and cretaceous. Am. J. Sci. 301, 112–149. https://doi.org/10.2475/ajs.301.2.112.

Jones, B., Manning, D.A.C., 1994. Comparison of geochemical indices used for interpretation of paleoredox conditions in ancient mudstones. Chem. Geol. 111, 111–129. https://doi.org/10.1016/0009-2541(94)90085-X.

Kuhnt, W., Holbourn, A., Moullade, M., 2011. Transient global cooling at the onset of early Aptian oceanic anoxic event (OAE) 1a. Geology 39 (4), 323–326. https://doi.org/10.1130/G31554.1.

Kump, L.R., Brantley, S.L., Arthur, M.A., 2000. Chemical weathering, atmospheric CO_2, and climate. Annu. Rev. Earth Planet. Sci. 28 (1), 611–667. https://doi.org/10.1146/annurev.earth.28.1.611.

Kuypers, M.M.M., van Breugel, Y., Schouten, S., Erba, E., Damsté, J.S.S., 2004. N_2-fixing cyanobacteria supplied nutrient N for cretaceous oceanic anoxic events. Geology 32 (10), 853–856. https://doi.org/10.1130/G20458.1.

Lechler, M., Pogge von Strandmann, P.A.B., Jenkyns, H.C., Prossera, G., Parente, M., 2015. Lithium-isotope evidence for enhanced silicate weathering during OAE1a (early Aptian Selli event). Earth Planet. Sci. Lett. 432, 210–222. https://doi.org/10.1016/j.epsl.2015.09.052.

Lorenzen, J., Kuhnt, W., Holbourn, A., Flögel, S., Moullade, M., Tronchetti, G., 2013. A new sediment core from the Bedoulian (lower Aptian) stratotype at Roquefort-La Bédoule, SE France. Cretac. Res. 39, 6–16. https://doi.org/10.1016/j.cretres.2012.03.019.

Martín-Chivelet, J., Berasategui, X., Rosales, I., Vilas, L., Vera, J.A., Caus, E., Gráfe, K.U., Mas, R., Puig, C., Segura, M., Robles, S., Floquet, M., Quesada, S., Ruiz-Ortiz, P.A., Frenegal-Martínez, M.A., Salas, R., García, A., Martín-Algarra, A., Arias, C., Meléndez, M., Chacón, B., Molina, J.M., Sanz, J.L., Castro, J.M., García-Hernández, M., Carenas, B., García-Hidalgo, J., Gil, J., Ortega, F., 2002. Cretaceous. In: Gibbons, W., Moreno, T. (Eds.), The Geology of Spain. The Geological Society, London, pp. 255–292.

Martínez-Rodríguez, R., Selby, D., Castro, J.M., de Gea, G.A., Nieto, L.M., Ruiz-Ortiz, P. A., 2021. Tracking magmatism and oceanic change through the early Aptian Anoxic Event (OAE 1a) to the late Aptian: Insights from osmium isotopes from the westernmost Tethys (SE Spain) Cau Core. Glob. Planet. Chang. 207, 103652. https://doi.org/10.1016/j.gloplacha.2021.103652.

Martínez-Rodríguez, R., Batenburg, S.J., Castro, J.M., de Gea, G.A., Nieto, L.M., Ruiz-Ortiz, P.A., Robinson, S., 2024. Integrated cyclostratigraphy of the Cau core (SE Spain) – a timescale for climate change during the early Aptian Anoxic Event (OAE 1a) and the late Aptian. Glob. Planet. Chang. 233, 104361. https://doi.org/10.1016/j.gloplacha.2024.104361.

Martínez-Ruiz, F., Kastner, M., Gallego-Torres, D., Rodrigo-Gámiz, M., Niero-Moreno, V., Ortega-Huertas, M., 2015. Paleoclimate and paleoceanography over the past 20,000 yr in the Mediterranean Sea Basins as indicated by sediment elemental proxies. Quat. Sci. Rev. 107, 25–46. https://doi.org/10.1016/j.quascirev.2014.09.018.

Masse, J.P., Bellion, Y., Benkhelil, J., Boulin, J., Cornee, J.J., Dercourt, J., Guiraud, R., Mascle, G., Poisson, A., Ricou, L.E., Sandulescu, M., 1993. Lower Aptian palaeoenvironments 114–112 Ma. In: Dercourt, J. (Ed.), Atlas Tethys Palaeoenvironmental Maps. Beceip-Franlab, Rueil-Malmaison.

Masse, J.P., Bouaziz, S., Amon, E.O., Baraboshkin, E., Tarkowski, R., Bergerat, F., 2000. Early Aptian (94.7–93.5 Ma). Peri-Tethys Palaeogeographical Atlas. In: Dercourt, J., Gaetani, M., Vrielynck, B., Barrier, E., Biju-Duval, B., Brunet, M.F., Cadet, J.P., Crasquin, S., Sandulescu, M. (Eds.), CCGM/CGMW, Paris (Map 13).

Matsumoto, H., Goto, K.T., Shimoda, G., Watanabe, Y., Shirai, K., Tejada, M.L.G., Ishikawa, A., Ando, A., Sano, T., Kuroda, J., Suzuki, K., 2024. Brief and intensive volcanic emissions from Ontong Java Nui heralded Oceanic Anoxic Event 1a. Commun. Earth Environ. 5 (1), 155. https://doi.org/10.1038/s43247-024-01310-0.

Méhay, S., Keller, C.E., Bernasconi, S.M., Weissert, H., Erba, E., Bottini, C., Hochuli, P.A., 2009. A volcanic CO_2 pulse triggered the cretaceous Oceanic Anoxic Event 1a and a biocalcification crisis. Geology 37, 819–822. https://doi.org/10.1130/G30100A.1.

Menegatti, A.P., Weissert, H., Brown, R.S., Tyson, R.V., Farrimond, P., Strasser, A., Caron, M., 1998. High-resolution $\delta^{13}C$ stratigraphy through the early Aptian "Livello Selli" of the Alpine Tethys. Paleoceanography 13, 530–545. https://doi.org/10.1029/98PA01793.

Molina, J.M., 1987. Análisis de Facies del Mesozoico en el Subbético Externo. (Prov. De Córdoba y sur de Jaén) [Ph.D. thesis]. University of Granada, Granada, p. 512.

Mutterlose, J., Bottini, C., Schouten, S., Sinninghe-Damsté, J.S., 2014. High Sea-surface temperatures during the early Aptian Oceanic Anoxic Event 1a in the Boreal Realm. Geology 42, 439–442. https://doi.org/10.1130/G35394.1.

Naafs, B.D.A., Pancost, R.D., 2016. Sea-surface temperature evolution across Aptian Oceanic Anoxic Event 1a. Geology 44, 959–962. https://doi.org/10.1130/G38575.1.

Naafs, B.D.A., Castro, J.M., De Gea, G.A., Quijano, M.L., Schmidt, D.N., Pancost, R.D., 2016. Gradual and sustained carbon dioxide release during Aptian Oceanic Anoxic Event 1a. Nat. Geosci. 9, 135–139. https://doi.org/10.1038/ngeo2627.

Naafs, B.D.A., Monteiro, F.M., Pearson, A., Higgins, M.B., Pancost, R.D., Ridgwell, A., 2019. Fundamentally different global marine nitrogen cycling in response to severe ocean deoxygenation. Proc. Natl. Acad. Sci. 116, 24979–24984. https://doi.org/10.1073/pnas.1905553116.

Naafs, B.D.A., Bianchini, G., Monteiro, F.M., Sánchez-Baracaldo, P., 2022. The occurrence of 2-methylhopanoids in modern bacteria and the geological record. Geobiology 20 (1), 41–59. https://doi.org/10.1111/gbi.12465.

Pagani, M., Caldeira, K., Archer, D., Zachos, J.C., 2006. An ancient carbon mystery. Science 314 (5805), 1556–1557. https://doi.org/10.1126/science.1136110.

Parker, M.S., Mock, T., Armbrust, E.V., 2008. Genomic insights into marine microalgae. Annu. Rev. Genet. 42, 619–645. https://doi.org/10.1146/annurev.genet.42.110807.091417.

Percival, L., Tedeschi, L., Creaser, R., Bottini, C., Erba, E., Giraud, F., Svensen, H., Savian, J., Trindade, R., Coccioni, R., 2021. Determining the style and provenance of magmatic activity during the early Aptian Oceanic Anoxic Event (OAE 1a). Glob. Planet. Chang. 200, 103461. https://doi.org/10.1016/j.gloplacha.2021.103461.

Percival, L.M.E., Matsumoto, H., Callegaro, S., Erba, E., Kerr, A.C., Mutterlose, J., Suzuki, K., 2025. Cretaceous large igneous provinces: From volcanic formation to Environmental catastrophes and biological crises. In: Hart, M.B., Batenburg, S.J., Huber, B.T., Price, G.D., Thibault, N., Wagreich, M., Walaszcayk, I. (Eds.), Cretaceous Project 200 Volume I: The Cretaceous World, 544, pp. 299–342. https://doi.org/10.1144/SP544-2023-88. Geological Society, London, Special Publications.

Peters, K.E., Walters, C.C., Moldowan, J.M., 2005. The Biomarker Guide, 2nd ed. Cambridge University Press, New York, p. 1155.

Peucker-Ehrenbrink, B., Ravizza, G., 2000. The marine osmium isotope record. Terra Nova 12, 205–219. https://doi.org/10.1046/j.1365-3121.2000.00295.x.

Polteau, S., Hendriks, B.W., Planke, S., Ganerød, M., Corfu, F., Faleide, J.I., Midtkandal, I., Svensen, H.S., Myklebust, R., 2016. The early cretaceous Barents Sea sill complex: distribution, $^{40}Ar/^{39}Ar$ geochronology, and implications for carbon gas formation. Palaeogeogr. Paleocllimatol. Palaeoecol. 441, 83–95. https://doi.org/10.1016/j.palaeo.2015.07.007.

Ricci, J.N., Morton, R., Kulkarni, G., Summers, M.L., Newman, D.K., 2017. Hopanoids play a role in stress tolerance and nutrient storage in the cyanobacterium *Nostoc punctiforme*. Geobiology 15 (1), 173–183. https://doi.org/10.1111/gbi.12204.

Rohmer, M., Bouvier-Nave, P., Ourisson, G., 1984. Distribution of hopanoid triterpenes in prokaryotes. Microbiology 130, 1137–1150. https://doi.org/10.1099/00221287-130-5-1137.

Sanchez-Hernandez, Y., Maurrasse, J.-M.R., 2016. The influence of regional factors in the expression of oceanic anoxic event 1a (OAE1a) in the semi-restricted Organyà Basin, south-Central Pyrenees, Spain. Palaeogeogr. Palaeoclimatol. Palaeoecol. 441, 582–598. https://doi.org/10.1016/j.palaeo.2015.06.031.

Schwark, L., Empt, P., 2006. Sterane biomarkers as indicators of palaeozoic algal evolution and extinction events. Palaeogeogr. Palaeoclimatol. Palaeoecol. 240, 225–236. https://doi.org/10.1016/j.palaeo.2006.03.050.

Skelton, P.W., 2003. The Cretaceous World. Cambridge University Press and The Open University, Cambridge, UK. Retrieved from. https://www.cambridge.org/tv/academic/subjects/earth–and–environmental–science/sedimentology–and–stratigraphy/cretaceous–world?format=HB#bookPeople.

Song, Y., Gilleaudeau, G.J., Algeo, T.J., Over, D.J., Lyons, T.W., Anbar, A.D., Xie, S.C., 2021. Biomarker evidence of algal-microbial community changes linked to redox and salinity variation, upper Devonian Chattanooga shale (Tennessee, USA). Geol. Soc. Am. Bull. 133 (1–2), 409–424. https://doi.org/10.1130/B35543.1.

Steuber, T., Alsuwaidi, M., Hennhoefer, D., Sulieman, H., AlBlooshi, A., McAlpin, T.D., Shebl, H., 2022. Environmental change and carbon-cycle dynamics during the onset of cretaceous oceanic anoxic event 1a from a carbonate-ramp depositional system. Abu Dhabi. U.A.E. Palaeogeogr. Palaeoclimatol. Palaeoecol. 601, 111086. https://doi.org/10.1016/J.PALAEO.2022.111086.

Summons, R.E., Jahnke, L.L., Hope, J.M., Logan, G.A., 1999. 2-Methylhopanoids as biomarkers for cyanobacterial oxygenic photosynthesis. Nature 400, 554–557. https://doi.org/10.1038/23005.

Sun, M.D., Lin, Q., Ramezani, J., Liu, J.S., Lu, Z.A., Yang, H.Q., Bai, J.H., Cai, S.X., Chen, J.C., Chen, X.Y., Cui, H., Deng, G.C., Gai, H.F., Gao, H.T., Guo, J., Guo, H., Hong, L.B., Hou, Y.S., Hua, Y.Y., Huang, L., Kong, K., Li, C.P., Liang, X.R., Liu, Z., Liu, L., Liu, B., Liu, S.L., Long, X.J., Lu, C., Lu, G.M., Luo, K., Ma, S.Y., Mo, F., Ouyang, Q.L., Shi, X.S., Sun, Z.Y., Sun, Y.Z., Tang, H., Tian, F., Wang, H.M., Wang, X., Wang, X., Wang, L.W., Wang, D., Wei, Y.X., Wu, W., Wu, C., Xiao, H., Yang, C.M., Yang, F., Yin, B.Y., Yu, X.X., Zhang, W.F., Zhang, Z.H., Zhao, R.P., Zheng, C.S., Zhou, Q., Zou, Z.Y., Cui, Z.X., Ma, Q., Ma, L., Zhu, J.X., Hu, J.F., Wei, G. J., Zhong, Y.T., Shen, Y.T., Shen, J., Zeng, T., Xu, Y.G., 2025. Terrestrial ecosystem response to early cretaceous global environmental change: a calibrated, high-resolution Aptian record from Northeast China. Earth Planet. Sci. Lett. 653, 119206. https://doi.org/10.1016/j.epsl.2025.119206.

Tejada, M.L.G., Suzuki, K., Kuroda, J., Coccioni, R., Mahoney, J.J., Ohkouchi, N., Tatsumi, Y., 2009. Ontong-Java Plateau eruption as a trigger for the early Aptian Oceanic Anoxic Event. Geology 37, 855–858. https://doi.org/10.1130/G25763A.1.

Van Breugel, Y., Schouten, S., Tsikos, H., Erba, E., Price, G.D., Damsté, J.S.S., 2007. Synchronous negative carbon isotope shifts in marine and terrestrial biomarkers at the onset of the early Aptian oceanic anoxic event 1a: evidence for the release of 13C-depleted carbon into the atmosphere. Paleoceanography 22, PA1210. https://doi.org/10.1029/2006PA001341.

Vera, J.A., 2004. Cordillera Bética y Baleares. In: Vera, J.A. (Ed.), Geología de España. Sociedad Geológica de España e Instituto Geológico y Minero de España, Madrid, pp. 345–464.

Wagner, T., Wallmann, K., Herrle, J., Hofmann, P., Stuesser, I., 2007. Consequences of moderate ~25,000 yr lasting emission of light CO_2 into the mid-cretaceous ocean. Earth Planet. Sci. Lett. 259, 200–211. https://doi.org/10.1016/j.epsl.2007.04.045.

Wedepohl, K.H., 1991. The composition of the upper Earth's crust and the natural cycles of selected metals. Metals in natural raw materials. Natural resources. In: Merian, E., Clarkson, T.W., Fishbein, I., Mallinckrodt, M.-G., Piscator, M., Schlipköter, H.W., Stoeppler, M., Stumm, W., Sunderman Jr., F.W. (Eds.), Metals and their Compounds in the Environment: Occurrence, Analysis, and Biological Relevance. VCH, Veinheim, New York, Basel, Cambridge, pp. 3–17.

Weissert, H., Erba, E., 2004. Volcanism, CO_2 and palaeoclimate: a Late Jurassic–Early Cretaceous carbon and oxygen isotope record. J. Geol. Soc. Lond. 161, 1–8. https://doi.org/10.1144/0016-764903-087.